




Splashing regimes of high-speed drop impact

Hui Wang¹ , Shuo Liu¹ , Annie-Claude Bayeul-Lainé¹ , David Murphy² , Joseph Katz³  and Olivier Coutier-Delgosha^{1,4} 

¹Univ. Lille, CNRS, ONERA, Arts et Metiers Institute of Technology, Centrale Lille, UMR 9014 - LMFL - Laboratoire de Mécanique des Fluides de Lille - Kampé de Fériet, F-59000 Lille, France

²Department of Mechanical Engineering, University of South Florida, Tampa, FL 33620, USA

³Department of Mechanical Engineering, Johns Hopkins University, 3400 N. Charles Street, Baltimore, MD 21218, USA

⁴Kevin T Crofton Department of Aerospace and Ocean Engineering, Virginia Tech, Blacksburg, VA 24060, USA

Corresponding authors: Hui Wang, hui.wang@ensam.eu; Olivier Coutier-Delgosha, ocoutier@vt.edu

(Received 1 May 2024; revised 29 July 2025; accepted 30 July 2025)

When a drop impinges onto a deep liquid pool, it can yield various splashing behaviours, leading to a crown-like structure along the free surface. Under high-speed impact conditions, the upper portion of the thin-walled crown may undergo necking and encapsulate a large bubble, which remains fascinating and is rarely discussed in the literature. In this work, we numerically study this physical process based on the volume-of-fluid and adaptive mesh refinement framework. Our meticulous observations have allowed us to unveil a spectrum of repeatable early-time jet behaviours, vorticity structures and crater evolution, underscoring the rich and complex nature of drop-impact phenomenon. We show that the interplay between aerodynamic pressure and surface tension on the liquid crown could play a significant role in its bending and surface closure. A regime map, incorporating both early-stage jet dynamics and overall bubble-canopy formation, is established across a wide parameter space. This study provides a comprehensive understanding of the diverse splashing regimes, offering insights into the fundamental characteristics of drop-impact phenomenon.

Key words: drops, gas/liquid flow, jets

1. Introduction

The ubiquitous phenomenon of drop impact plays a vital role in numerous natural and technological processes, influencing a diverse array of occurrences from surface erosion

and soil stability to the performance of advanced manufacturing techniques. In the natural realm, raindrops influence the response of plant surfaces and the transmission of seeds and pathogens (Kim *et al.* 2019; Bourouiba 2021; Roth-Nebelsick *et al.* 2022), the spreading of petroleum contaminants (Murphy *et al.* 2015; Castillo-Orozco *et al.* 2016) and soil and structure erosion (Assouline 2004; Zhou *et al.* 2009; Fernández-Raga *et al.* 2017; Lardier *et al.* 2019). In the realm of industrial applications, it plays a crucial role in processes such as spray injecting and cooling (Breitenbach, Roisman & Tropea 2018; Wang *et al.* 2020; Benthier *et al.* 2021), inkjet printing (Lohse 2022), agriculture irrigation (Gart *et al.* 2015; Gilet & Bourouiba 2015) and internal combustion engines (Panao & Moreira 2005; Moreira, Moita & Panao 2010). Scientific research aimed at uncovering the internal mechanisms and fundamental physics of drop impact thus holds immense potential in facilitating various technical applications where this process is involved, but remains challenging due to increased complexities of multiscale physics and interfacial flows (Deegan, Brunet & Eggers 2007).

Since the pioneering works of Worthington (1883, 1895) more than a century ago, different scenarios of drop impact, including solid target (Josserand & Thoroddsen 2016; Jian *et al.* 2018), thin and shallow liquid film (Mukherjee & Abraham 2007; Coppola *et al.* 2011; Sykes *et al.* 2023), deep liquid pool (Murphy *et al.* 2015; Ray, Biswas & Sharma 2015; Michon, Josserand & Séon 2017), miscible or immiscible liquids (Lhuissier *et al.* 2013; Castillo-Orozco *et al.* 2016; Lherm *et al.* 2022) and normal or oblique angle (Leneweit *et al.* 2005; Gielen *et al.* 2017; Liu 2018), have been categorised and documented in the literature (Rein 1993; Yarin 2006; Liang & Mudawar 2016). For normal (perpendicular) drop impact onto the deep volume of the same liquid, three dimensionless parameters are usually used to characterise the splashing dynamics, namely the Froude number $Fr = U_0/\sqrt{gd}$, the Reynolds number $Re = \rho_l U_0 d/\mu_l$ and the Weber number $We = \rho_l U_0^2 d/\sigma$, where U_0 is the impact speed, d the drop diameter, g the gravitational acceleration, ρ_l the liquid density, μ_l the liquid dynamic viscosity, and σ the liquid surface tension.

In the regime of splashing, significant progress has been made in delineating its early-stage morphological behaviours over the past decades. As the drop touches the pool, a thin liquid ejecta is shot out horizontally from the connection of two masses due to localised pressure buildup (Weiss & Yarin 1999; Thoroddsen 2002; Josserand & Zaleski 2003; Howison *et al.* 2005; Josserand, Ray & Zaleski 2016) and expands rapidly outwards, resulting in a series of rich splashing processes afterwards. In some cases ($2000 < Re < 6000$), the base of the ejecta may oscillate, shedding a vortex that later lifts a ‘lamella’ (Zhang *et al.* 2012; Agbaglah *et al.* 2015; Sykes *et al.* 2023) or propelling the ejecta to bend and collide with the surfaces of drop or pool (Thoroddsen *et al.* 2011; Agbaglah *et al.* 2015; Tian *et al.* 2024), potentially entrapping a large toroidal bubble in the substrate liquid (Thoroddsen 2002; Deegan *et al.* 2007). For the highest range of Re , the most unstable splashing mode occurs and the ‘emerging-rupturing-ejecta’ is observed (Thoroddsen 2002), where the ejecta interacts strongly with the free surfaces, entrapping a row of toroidal bubbles inside the liquid tank (Castrejón-Pita *et al.* 2012; Thoraval *et al.* 2012). Despite the improved understanding of the initial jet multiplicity owing to the enhanced capabilities in both experimental and numerical approaches, the intricate interplays between jets and free surfaces remain fascinating, and the critical conditions that determine the transitions between different splashing behaviours are still not well elucidated.

After the initial stage, a typical drop-impingement-induced structure, composed of a submerging cavity surrounded by a thin-walled liquid crown, is formed. It is well established in the literature that the overall morphology during this period depends greatly

on the impact parameters. When the drop impinges at very low energy, a thick tongue (swell) is generated along the drop–pool connection and the drop coalesces with the receiving bulk (Chapman & Critchlow 1967; Rodriguez & Mesler 1985, 1988; Mohamed-Kassim & Longmire 2004). For slightly higher impact energy, a flared liquid crown rises up cylindrically along the periphery of a semispherical cavity (Fedorchenko & Wang 2004; Ray *et al.* 2015). Further increasing the impact energy, the crown is more developed, and liquid ligaments are stretched out of its upper rim, producing and sending out secondary droplets into the air (Okawa, Shiraishi & Mori 2006; Deegan *et al.* 2007; Guildenbecher *et al.* 2014; Wu, Wang & Zhao 2020). For these abovementioned cases, after the crown (swell) reaches its maximum position, capillary ripples start to propagate on the interior wall of the crater and subsequently lead to the collapse of the structure, resulting in an axial upward jet rising out of the cavity bottom, known as the ‘Worthington jet’ (Ray *et al.* 2015; Michon *et al.* 2017).

In the most energetic regime of drop impact, the crown undergoes further elevation and its upper edge necks in before retraction, encapsulating a large gas volume within it (Worthington 1883), which is qualitatively different from the phenomena already mentioned. Upon surface closure, an upward jet and a downward jet protrude from the closure point due to a large axial pressure gradient. The formation of similar vertical jets is also a subject of intense study in other physical processes, such as rapid boiling (Marston & Li 2019) and cavitation (Saade *et al.* 2021). The downward jet then moves towards the cavity bottom and eventually mixes with the upward-rising jet coming from the cavity floor (Engel 1966). During the final stages, a thin-filmed bubble forms over the pool surface, ultimately breaking up due to combined effects of surface tension and external disturbances (Motzkus, Gensdarmes & Géhin 2009; Murphy *et al.* 2015). The importance of understanding such physical processes under high-energy impact conditions was evidenced by Murphy *et al.* (2015) in the context of post-oil-spill accidents on the ocean surface, where additional spraying sources of marine aerosols (Dasouqi, Yeom & Murphy 2021) could be introduced by the impact of raindrops or use of oil dispersant, which could therefore cause adverse effects on the environment, economy and public health.

For drop impact on thin liquid layers, previous studies have provided some quantitative investigations of the critical conditions for large-bubble encapsulation at high-impact velocities (Pan *et al.* 2008; Pan & Hung 2010; Geppert *et al.* 2016; Aljedaani *et al.* 2018; Ribeiro *et al.* 2023a,b), focusing primarily on the effects of liquid-film thickness and underlying material on the splash. In such scenarios, the growth of the submerging cavity is greatly inhibited by the finite liquid film, and the interactions between the enlarging cavity and the underlying wall are crucial factors influencing the closure event (Pan *et al.* 2008). However, in the case of deep receiving pools, the cavity undergoes rapid expansion predominantly in the vertical direction, independent of the presence of walls. As a result, the cavity takes on a hemispherical shape (Engel 1966, 1967; Bisighini *et al.* 2010; Murphy *et al.* 2015; Sochan *et al.* 2018). This distinct crater morphology therefore gives rise to different characteristics and dynamics in the process of bubble-canopy (BC) formation compared with scenarios impacting thin liquid films.

Notably, while certain studies have mentioned the phenomenon of BC formation in deep receiving pools within the context of underwater noise (Medwin *et al.* 1992; Prosperetti & Oguz 1993), crater expansion (Worthington 1883; Engel 1966, 1967; Bisighini *et al.* 2010), marine aerosols (Murphy *et al.* 2015) and Rayleigh–Taylor instability (Lherm *et al.* 2021), limited attention has been devoted to investigating the underlying determinants of this specific phenomenon. The influence of liquid viscosity and surface tension on the characteristic behaviours of the closure event has been initiated (Murphy *et al.* 2015;

Sochan *et al.* 2018), yet the critical transitional criteria are unsettled and the mechanisms of surface closure remain to be understood. Therefore, in this paper, we study the dynamics of drop impact on the deep pool of the same liquid using direct numerical simulations. Various splashing behaviours, spanning from gentle coalescence to the most energetic splash of BC, are investigated by systematically varying the dimensionless Reynolds and Weber numbers. A comprehensive regime map of drop splash that incorporates both early-time jet dynamics and BC formation, covering a broad parameter space of $1000 \leq Re \leq 30000$ and $100 \leq We \leq 3000$, is therefore concluded.

The paper is organised as follows. In § 2, we describe the governing equations, numerical approaches and general numerical set-ups. In § 3, detailed comparisons between numerical and experimental results are conducted. In § 4, we present numerical investigations of splashing dynamics under varied impact conditions. The paper ends with the conclusions in § 5.

2. Numerical methods

2.1. Governing equations

To simulate the drop-impact gas–liquid system, we solve the two-phase incompressible Navier–Stokes equations with respective densities (ρ_g , ρ_l) and viscosities (μ_g , μ_l) (subscript g and l denote the properties in the gas and in the liquid, respectively):

$$\nabla \cdot \mathbf{U} = 0, \quad (2.1)$$

$$\rho \left(\frac{\partial \mathbf{U}}{\partial t} + (\mathbf{U} \cdot \nabla) \mathbf{U} \right) = -\nabla P + \nabla \cdot (2\mu \mathbf{D}) + \rho \mathbf{a} + \sigma \kappa \delta_s \mathbf{n}, \quad (2.2)$$

where \mathbf{U} is the velocity vector, t is time, P is the pressure, $\mathbf{D} = [\nabla \mathbf{U} + (\nabla \mathbf{U})^T]/2$ is the deformation tensor, \mathbf{a} is the body force along the impact direction, δ_s is the Dirac function indicating the interface, and σ , κ , \mathbf{n} are the surface tension, curvature and normal vector of the interface, respectively. The density ρ and viscosity μ take constant values in each phase.

We choose the reference values of drop diameter d , initial impact speed U_0 , liquid density ρ_l and gravitational acceleration g to non-dimensionalise the Navier–Stokes equations. Therefore, the dimensionless variables scaled by the characteristic quantities are

$$\hat{\mathbf{X}} = \frac{\mathbf{X}}{d}, \quad \hat{\mathbf{U}} = \frac{\mathbf{U}}{U_0}, \quad \hat{t} = \frac{tU_0}{d}, \quad \hat{P} = \frac{P}{\rho_l U_0^2}, \quad \hat{\mathbf{a}} = \frac{\mathbf{a}}{g}, \quad \hat{\kappa} = \kappa d, \quad \hat{\delta}_s = \delta_s d. \quad (2.3)$$

where \mathbf{X} is the three-dimensional coordinates. We substitute these dimensionless variables into the governing equations. Then (2.2) can be rewritten as

$$\frac{\partial \hat{\mathbf{U}}}{\partial \hat{t}} + (\hat{\mathbf{U}} \cdot \nabla) \hat{\mathbf{U}} = -\nabla \hat{P} + \frac{1}{Re} \nabla \cdot (2\mathbf{D}) + \frac{1}{Fr^2} \hat{\mathbf{a}} + \frac{1}{We} \hat{\kappa} \hat{\delta}_s \mathbf{n}. \quad (2.4)$$

This final form incorporates three dimensionless numbers:

$$Re = \frac{\rho_l d U_0}{\mu_l}, \quad We = \frac{\rho_l d U_0^2}{\sigma}, \quad Fr = \frac{U_0}{\sqrt{gd}}, \quad (2.5)$$

where the Reynolds number (Re), Weber number (We) and Froude number (Fr) represent ratios of inertial forces to viscous, surface tension and gravitational forces, respectively. These dimensionless numbers are crucial for understanding the dominant physical mechanisms governing fluid flows and classifying various splashing behaviours.

2.2. Numerical solver

We use the open-source Basilisk C (Popinet & collaborators 2013–2025) to solve the two-phase flow system. The momentum conserving volume-of-fluid (VOF) numerical scheme is employed here (Fuster & Popinet 2018). The gas–liquid interface is tracked and reconstructed using the VOF method (Scardovelli & Zaleski 1999), and the volume fraction $f(X, t)$ of the first fluid (liquid) is advected and described as follows:

$$\frac{\partial f}{\partial t} + \nabla \cdot (f\mathbf{U}) = 0, \quad f(X, t) = \begin{cases} f = 1 & \text{for liquid} \\ 0 < f < 1 & \text{for interface} \\ f = 0 & \text{for gas.} \end{cases} \quad (2.6)$$

The local density and viscosity in the computational domain then can be computed by the arithmetic means using $\rho(f) = f\rho_l + (1 - f)\rho_g$ and $\mu(f) = f\mu_l + (1 - f)\mu_g$. The surface tension is calculated using the continuum surface force (CSF) model described in Francois *et al.* (2006). The tree-based structure of spatial discretisation and adaptive mesh refinement (AMR) techniques (Van Hooft *et al.* 2018) are applied to adaptively follow the smallest structures of the flow, thus concentrating the computational resources on the most concerning regions. Starting from a ‘parent’ cell at level 0, four ‘children’ cells are generated at level 1 in two dimensions. Various levels of local refinement can be present within the spatial domain at the same time. With the maximum level of refinement $L_{max} = n$, the finest resolution in each dimension is reduced to $1/2^n$ of the initial computational domain. The grid is refined or coarsened adaptively based on the wavelet-estimated spatially discretised field errors using AMR. The Basilisk solver has been validated extensively on the problems with multiphase complex flows as can be found in Popinet & collaborators (2013–2025).

All the numerical results presented in the main text of this paper were performed on 128 cores using the computational resources at the Advanced Research Computing (ARC) at Virginia Tech.

2.3. Axisymmetric flow configurations

In the literature, the shape of the impact drop before contact was widely assumed as a sphere (Berberović *et al.* 2009; Thoraval *et al.* 2012; Agbaglah *et al.* 2015; Ray *et al.* 2015; Fudge *et al.* 2021; Wu *et al.* 2021), but this may not be the fact in many situations (Soni *et al.* 2020). In real experiments, right after leaving the nozzle of the injector, the drop will fall freely through the surrounding gas to accelerate to a certain impact velocity. During this displacement, significant deformation might be observed depending on various factors (liquid properties, drop size, temperature and surrounding gas) (Volkov, Kuznetsov & Strizhak 2015), which would accordingly alter the physical dynamics of the impact (Scolan & Korobkin 2001; Thoraval, Li & Thoroddsen 2016). Particularly, the shape versus height oscillation was tested and modelled by Thoraval *et al.* (2013), who highlighted the relevance of pinch-off oscillations to the dynamics of the impact. In our current study, we define the drop as an oblate shape based on the experimental measurements of Murphy *et al.* (2015). The initial horizontal and vertical diameters of the drop are given as $d_h = 4.3$ mm and $d_v = 3.8$ mm, thus resulting in an effective drop diameter calculated as $d = (d_v d_h^2)^{1/3} = 4.1$ mm.

In this study, simulations are performed in axisymmetric configurations as shown in figure 1. The computational domain is a square (cylinder in axisymmetric coordinates) and the side length of the domain is $L = 20d$. The free surface of the pool is located in

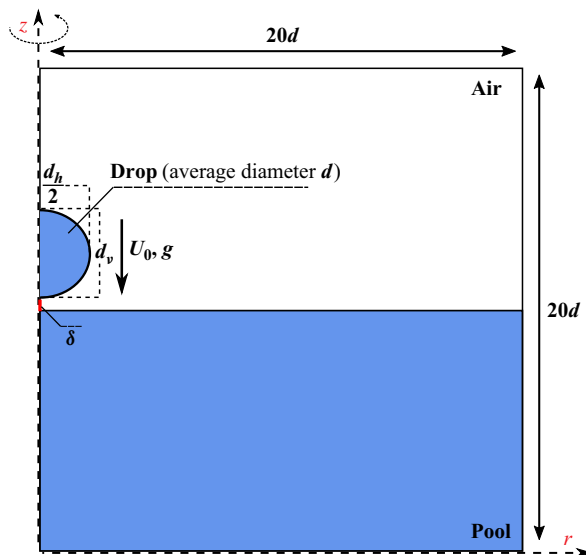


Figure 1. Axisymmetric configurations for the simulation of drop impact on the same liquid pool. The blue represents the heavier fluid (e.g. water) and the white represents the lighter one (e.g. air). The dimensions shown here are not to scale.

the middle of the axial direction and the depth of the pool is $H = 10d$, providing sufficient space for crater development while minimising boundary influences (see discussion in [Appendix B](#)). The initial gap between drop and pool is $\delta = 0.1d$, which allows taking the effects of air sheet entrapment into account. The free outflow boundary conditions are imposed on the top of the domain, while the default symmetry boundary conditions are applied for the other three boundaries. At the initial time, the mesh around the drop and the free surface of the pool is refined at the maximum refinement level, and the mesh is gradually coarsened away from the interfaces, which promises a good geometric description of the drop and free surface at the beginning. During the simulations, grids are adapted based on the wavelet-estimated errors of the volume fraction (tolerance $f_{err} = 1e-4$) and velocity (tolerance $u_{err} = 1e-2$) fields using AMR. The effect of gravitational force is taken into consideration in this study.

As discussed in [Appendix A](#), our preliminary mesh study has found that a minimum grid resolution of at least 1638 cells per drop diameter, corresponding to a maximum refinement level at $L_{max} = 15$, is necessary for capturing the ‘irregular splash’ regime induced by the most energetic drop impact at the highest Re and We range. The ‘primary splashing features’ are approximately grid-converged at $L_{max} = 15, 16$ and 17 . Hence, in the main text of this manuscript, all the numerical results are obtained using the maximum refinement level $L_{max} = 15$, for the purpose of parametric investigation through a broad range of parameter space. The minimum level of refinement is fixed to $L_{min} = 7$ during calculations.

It should be noted that this work is aimed to capture the primary features of high-speed drop impact that are considered symmetric. For those who are interested in analysing the non-symmetric phenomena such as neck instabilities, crown fragmentation, droplet statistics and motion of central jet, full three-dimensional simulations are strongly suggested (Wang *et al.* 2023). All the data hereafter are scaled by the initial drop diameter d and the impact speed U_0 , thus the time is scaled as $\hat{t} = tU_0/d$.

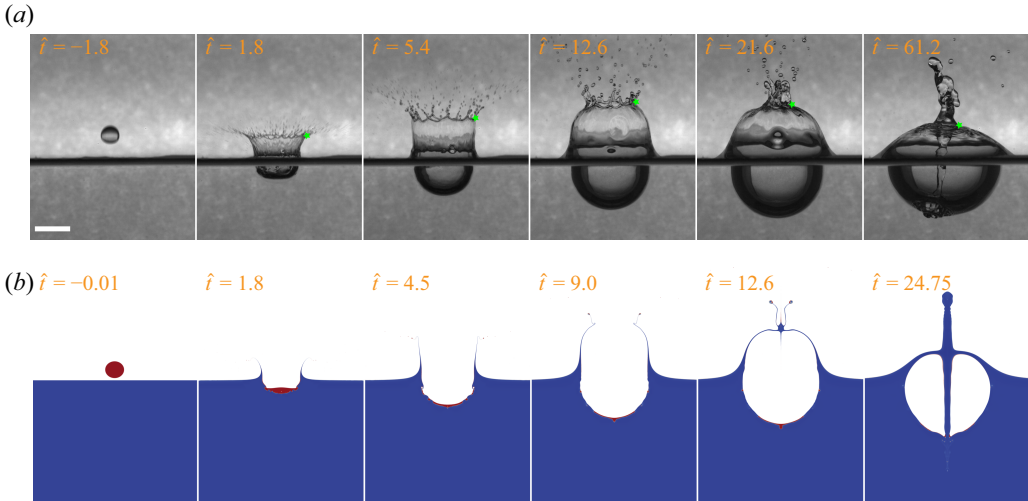


Figure 2. Typical sequence of splashing events for a water drop impacting a deep water pool. The drop for experiment and simulation has the same parameters: $d_h = 4.3$ mm, $d_v = 3.8$ mm and $U_0 = 7.2$ m s⁻¹ ($Re = 30\,060$, $We = 2964$). The experiment and simulation are presented with the same scale. The scale bar is $2.0d$ long, where $d = 4.1$ mm. The images in (a) are extracted from one of the replicated counterparts of the control case in Murphy *et al.* (2015), and the snapshots in (b) are produced by our axisymmetric simulation. The green asterisks indicate the tracked positions of the upper rim of the crown in the experiment. The red and blue colours in the simulation represent the fluids from the drop and the pool respectively. See supplementary movie 1 available at <https://doi.org/10.1017/jfm.2025.10543>.

3. Comparisons with experiment

This section numerically reproduces one particular case of a water drop impacting a deep water pool. Detailed comparisons between numerical results and available experimental data from Murphy *et al.* (2015) are performed to validate the employed numerical schemes in the present study. In this calculation, artificial seawater is used for both the drop and pool, since the properties of the liquids in the drop and pool are almost the same, and air for the surrounding gas. The properties of seawater are density $\rho_l = 1018.3$ kg m⁻³, dynamic viscosity $\mu_l = 1.0 \times 10^{-3}$ N s m⁻² and surface tension $\sigma = 73.0 \times 10^{-3}$ N m⁻¹. The drop is initialised with $d_h = 4.3$ mm, $d_v = 3.8$ mm and $U_0 = 7.2$ m s⁻¹, as same as the experimental measurements in Murphy *et al.* (2015). This leads to a drop impact set-up at $Re = 30\,060$ and $We = 2964$, corresponding to the highest parameters investigated in this study.

3.1. Morphology and kinematics

Figure 2 shows a typical sequence of the event produced by high-speed raindrops impacting the ocean surface. It can be seen that the simulation successfully reproduced most of the distinctive physical features observed by the high-speed camera, including the formation of an initial outward-expanding crown around a disk-like cavity ($\hat{t} = 1.8$), the transition of the orientation of the crown rim from horizontal-outward to vertical-upward along with the growth of a hemispherical cavity ($\hat{t} = 4.5$), the inward bending of the upper portion of the crown ($\hat{t} = 9.0$), the formation of BC and the protrusion of vertical jets from the closure point due to localised pressure buildup ($\hat{t} = 12.6$), and finally the impingement of the downward central jet to the cavity bottom ($\hat{t} = 24.75$). An overall good qualitative comparison is obtained. It is also worth noting that an elliptic pattern can be observed in the experimental images at certain instances (e.g. $\hat{t} = 5.4, 12.6, 21.6$). This feature is caused by lensing effects, where the curvature of the crown acts as a lens, refracting light

and producing the observed pattern. As the crown evolves dynamically, changes in the local surface curvature can alter the position of the lensing effect, leading to its shifting appearance in different frames.

To further verify our current numerical strategies, [figure 3](#) presents a comparison between various quantities extracted from axisymmetric simulation and experiment. In the experiments of Murphy *et al.* (2015), the crown rim position is defined as the outer edge of the crown neck where ligaments are formed, as indicated by green asterisks in [figure 2](#). In our axisymmetric simulation, the trajectory of the crown neck position (\tilde{R}_r , \tilde{R}_h) is assessed using the diagrams depicted in [figure 3\(a\)](#). During the crown outward-expanding phase, the crown neck position corresponds to the highest point on the crown interface, as sketched at $\hat{t} = 3.6$ in [figure 3\(a\)](#). In the inward-bending surface closure phase, we track the point on the crown surface closest to the axis of symmetry, as sketched at $\hat{t} = 9.45$ in [figure 3\(a\)](#). The cavity depth (\tilde{C}_d) and width (\tilde{C}_r) are monitored by tracking the lowest position of the cavity and the cavity's horizontal radius along the initial quiescent free surface of the pool, respectively.

As shown in [figure 3\(b\)](#), the numerical results for crown neck kinematics show a generally similar trend to the experimental measurements. However, the advancement of the impact in axisymmetric simulation evolves more rapidly compared with real experiments, leading to the accelerated growth of the upper crown and earlier occurrence of bubble closure, as clearly shown in the temporal evolution of \tilde{R}_r and \tilde{R}_h in [figures 3\(c\)](#) and [3\(d\)](#). This discrepancy arises from the absence of strong three-dimensional phenomena along the thickened crown rim, as discussed in detail in § 3.2. The discrepancy in crown evolution could accordingly alter the development of the subsurface cavity. [Figures 3\(e\)](#) and [3\(f\)](#) plot the temporal evolution of the cavity dimensions (\tilde{C}_r , \tilde{C}_d), revealing general good agreement between numerical and experimental results before closure. For highly energetic impacts like the present case, the cavity remains in its expanding phase after the closure of the upper crown ($\hat{t} > 12.6$ in simulation), thereby drawing gas into the subsurface cavity by pulling the bubble ceiling downwards. As a result, the cavity expansion along the free surface of the receiving pool is significantly impeded as illustrated in [figure 3\(e\)](#). This suggests that an earlier surface closure event would hinder the development of cavity. Interestingly, in the experimental study of Mansoor *et al.* (2014), further extended cavities were achieved and examined by artificially eliminating this surface closure process for the impacts of superhydrophobic spheres onto the deep liquid pool. The depth of the cavity, as shown in [figure 3\(f\)](#), except for minor disturbances caused by the impingement of the downward-moving jet, follows a similar trend in both the numerical and experimental results.

3.2. Limitations of axisymmetric simulation

In the aforementioned comparisons, a noticeable phase difference in the timing of crown growth and closure event is observed between our axisymmetric simulation and experimental observations. Specifically, the simulation exhibits faster growth and closure of the upper crown compared with the experiments. This discrepancy can be attributed to the inherent limitations of axisymmetric approaches. In real-world phenomena, during high-speed drop impact, crown development is determined by a three-dimensional rim that preserves strong transverse instabilities followed by corrugation formation and continuous droplet shedding (Roisman, Horvat & Tropea 2006; Deegan *et al.* 2007; Murphy *et al.* 2015). This complex dynamics gives rise to intricate flow patterns and additional interactions with the surrounding environment within the upper crown, which plays a crucial role in delaying the development of the structure (Wang *et al.* 2023). However, in

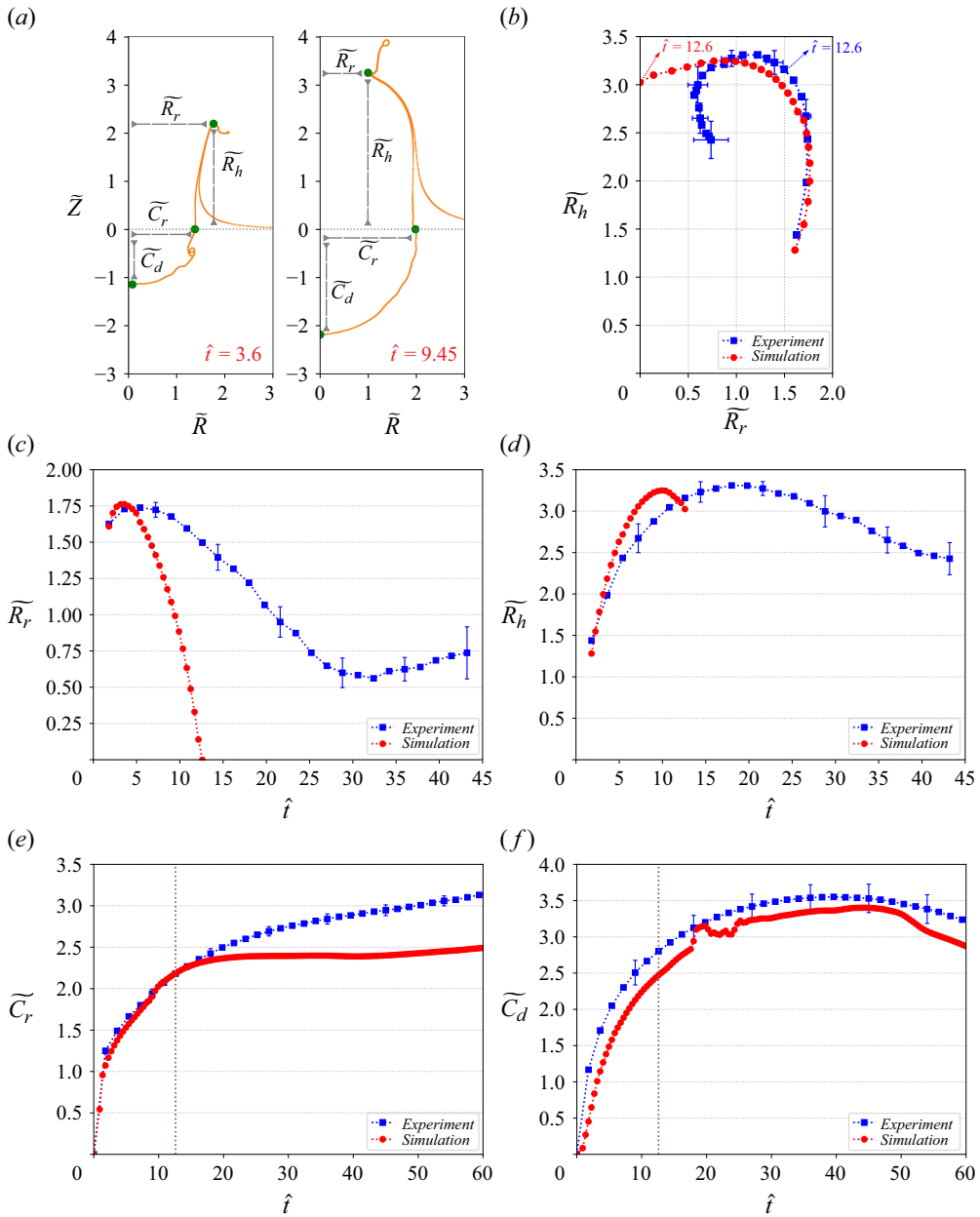


Figure 3. Quantitative comparisons of axisymmetric numerical results with experimental measurements of Murphy *et al.* (2015). (a) Sketch of the tracked quantities: crown neck position (\tilde{R}_r , \tilde{R}_h), cavity dimensions (\tilde{C}_r , \tilde{C}_d). The radial and axial coordinates are rescaled by d as \tilde{R} and \tilde{Z} . (b) Trajectory of the crown neck position. The first point is at $\hat{t} = 1.8$. The time delay in experimental data between points is $\hat{t} = 12.6$, and the time delay in numerical results is $\hat{t} = 0.45$. (c) Time evolution of the crown neck radius (\tilde{R}_r). (d) Time evolution of the crown neck height (\tilde{R}_h). (e) Time evolution of the cavity width (\tilde{C}_r). (f) Time evolution of the cavity depth (\tilde{C}_d). The vertical dotted lines indicate the timing of the crown closure in axisymmetric simulation. The error bars indicate the standard deviation in experimental data.

axisymmetric simulations, the upper part of the crown evolves into a very thin and highly sensitive interface, serving as the determining factor for the crown dynamics and closure event. The absence of these three-dimensional effects in axisymmetric simulations eventually leads to an underestimation of the time required for the crown to develop and enclose, compared with the experimental observations.

Furthermore, the calculation of the downward-moving jet protruding from the closure point affects the subsequent dynamics. In reality, this jet arises from the rapid local pressure buildup due to the convergence of crown rims from all directions. Previous experiments have clearly demonstrated the non-axisymmetric footprint of this central jet and the off-centre point where it pierces the cavity (Bisighini *et al.* 2010; Murphy *et al.* 2015), indicating that the jet kinematics is greatly influenced by three-dimensional effects. However, this physical process cannot be accurately captured by an axisymmetric configuration, as the jet is only composed of flows along the symmetry plane. As a consequence, the jet in axisymmetric simulation is confined to attach to the symmetry axis and rapidly penetrates the bottom of the cavity floor ($\hat{t} = 24.75$ in figure 2), thereby further accelerating the impact process.

While acknowledging the limitations and simplifications made in the model, axisymmetric simulations remain an effective tool for studying drop-impact phenomena and it has provided valuable insights into the understanding of splashing dynamics, as evidenced by previous studies (Thoraval *et al.* 2012; Agbaglah *et al.* 2015; Josserand *et al.* 2016; Thoraval *et al.* 2016; Deka *et al.* 2017; Jian *et al.* 2020; Fudge *et al.* 2021, 2023; Sykes *et al.* 2023; Osama, Deegan & Agbaglah 2024). It is important to emphasise that the main objective of this study is to perform a comprehensive study of drop-impact dynamics across a wide range of parameter space, focusing on those phenomena that exhibit approximate axisymmetry. The validation conducted in § 3.1 has demonstrated its ability to reproduce key splashing features in the process of high-speed drop impact, which is sufficient to support the systematic study conducted in the following sections.

4. Results and discussion

The splashing dynamics of drop impact, as described in § 2.1, depends primarily on several dimensionless parameters. In this parametric study, we maintain the values of $\rho_l/\rho_g = 783$, $\mu_l/\mu_g = 56$, $d_h = 4.3$ mm, $d_v = 3.8$ mm and $U_0 = 7.2$ m s⁻¹ constant. The effect of dimensionless Reynolds and Weber numbers are explored for $1000 \leq Re \leq 30\,000$ and $100 \leq We \leq 3000$ by systematically varying the liquid viscosity μ_l and surface tension σ . Through this variation, we investigate and analyse the diverse splashing behaviours exhibited during high-speed drop-pool impingement.

Figure 4 presents a comprehensive regime map illustrating various distinctive drop-impact dynamics observed in our simulations. In this map, we encompass both the early-time jet behaviours and overall evolution of the crater structure, which, to the best of the authors' knowledge, should be first reported herein. Based on our axisymmetric simulations, a wide variety of repeatable behaviours of early jets (see figure 5) and modes of crater evolution (see figure 9) have been identified, underscoring the rich and complex nature of splashing phenomenon. The presented map is the outcome of conducting more than 800 simulations.

4.1. Early-time jet behaviours

This section focuses on the early-time jet dynamics in the vicinity of the neck region formed between the downward-impinging drop and the receiving pool. This comprises

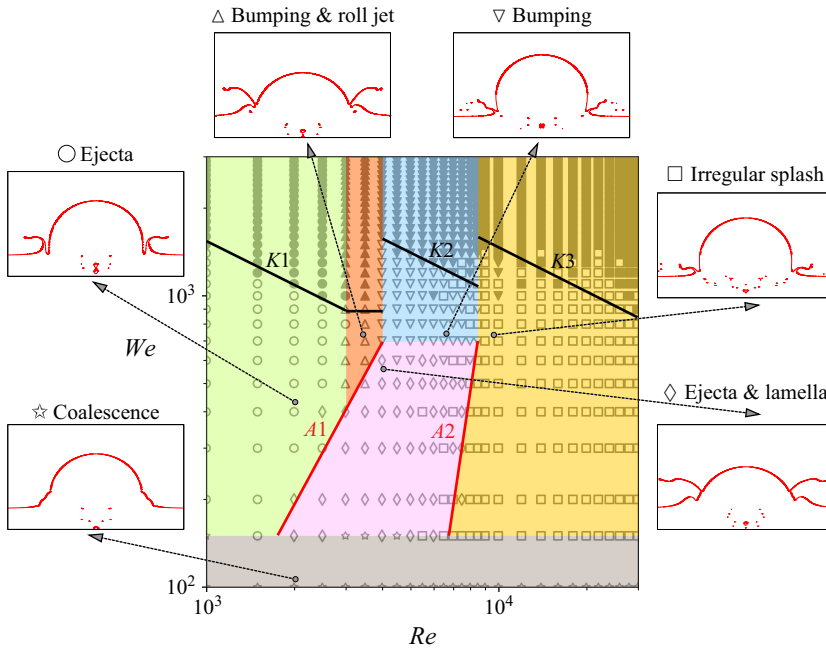


Figure 4. Regime map of drop impact in terms of dimensionless Reynolds (Re) and Weber (We) numbers, showing transitions between various splashing behaviours identified in the present investigation. The filled symbols represent BC formation, whereas the hollow symbols indicate that the crown does not enclose. The solid black lines determine the limit values of BC formation at different ranges of Re fitted based on the simple relation $K = We\sqrt{Re}$: $K1 = 4.9 \times 10^4$, $K2 = 9.9 \times 10^4$ and $K3 = 14.7 \times 10^4$. The solid red lines $A1$ and $A2$ indicate the approximate limits between different jet behaviours. Insets show representative impact cases for each regime, with arrows pointing from the impact condition to the corresponding case: ☆ coalescence → $Re = 2000$, $We = 100$; ○ ejecta → $Re = 2000$, $We = 400$; ◇ ejecta & lamella → $Re = 4000$, $We = 600$; △ bumping & roll jet → $Re = 3500$ and $We = 700$; ▽ bumping → $Re = 6500$ and $We = 700$; □ irregular → $Re = 9500$ and $We = 700$.

several key splashing regimes depicted in figure 4, including ☆ coalescence, ○ ejecta formation, ◇ ejecta with a late-emerging lamella, ▽ bumping between ejecta and drop interface, △ bumping with secondary roll jet formation, and □ irregular splash with strong interfacial interactions. Figure 5 illustrates seven representative cases calculated under different impact conditions, showing various repeatable jet shapes and vorticity structures captured by our simulations (see supplementary movie 2).

At $We < 150$, the very high surface tension generally prevents the emergence of the ejecta jet and the drop coalesces gently with the substrate fluid (☆ coalescence regime in figure 4). As the drop sinks and spreads, a large vortex is subsequently detached from the upper corner of the connection and travels horizontally underneath the free surface, generating a capillary swell that propagates on the interface (see figure 5a for a case with $Re = 2000$, $We = 100$). A similar ‘no-jet’ boundary at $We \approx 200$ was also observed in previous experimental (Zhang *et al.* 2012) and numerical (Agbaglah *et al.* 2015) investigations. For $Re < 3000$ and $We > 150$, the formation of thin ejecta starts to be observed in the neck of the connection between two liquid masses (○ ejecta regime in figure 4), as illustrated in figure 5(b) for a case with $Re = 2500$ and $We = 300$.

Increasing the Reynolds number to $Re \approx 2000 \sim 9000$, intriguing jet behaviours are categorised. As shown in figure 5(c) ($Re = 4000$, $We = 400$), a vorticity structure of one sign is generated at the upper corner of the ejecta ($\hat{t} = 0.1656$). However, compared with

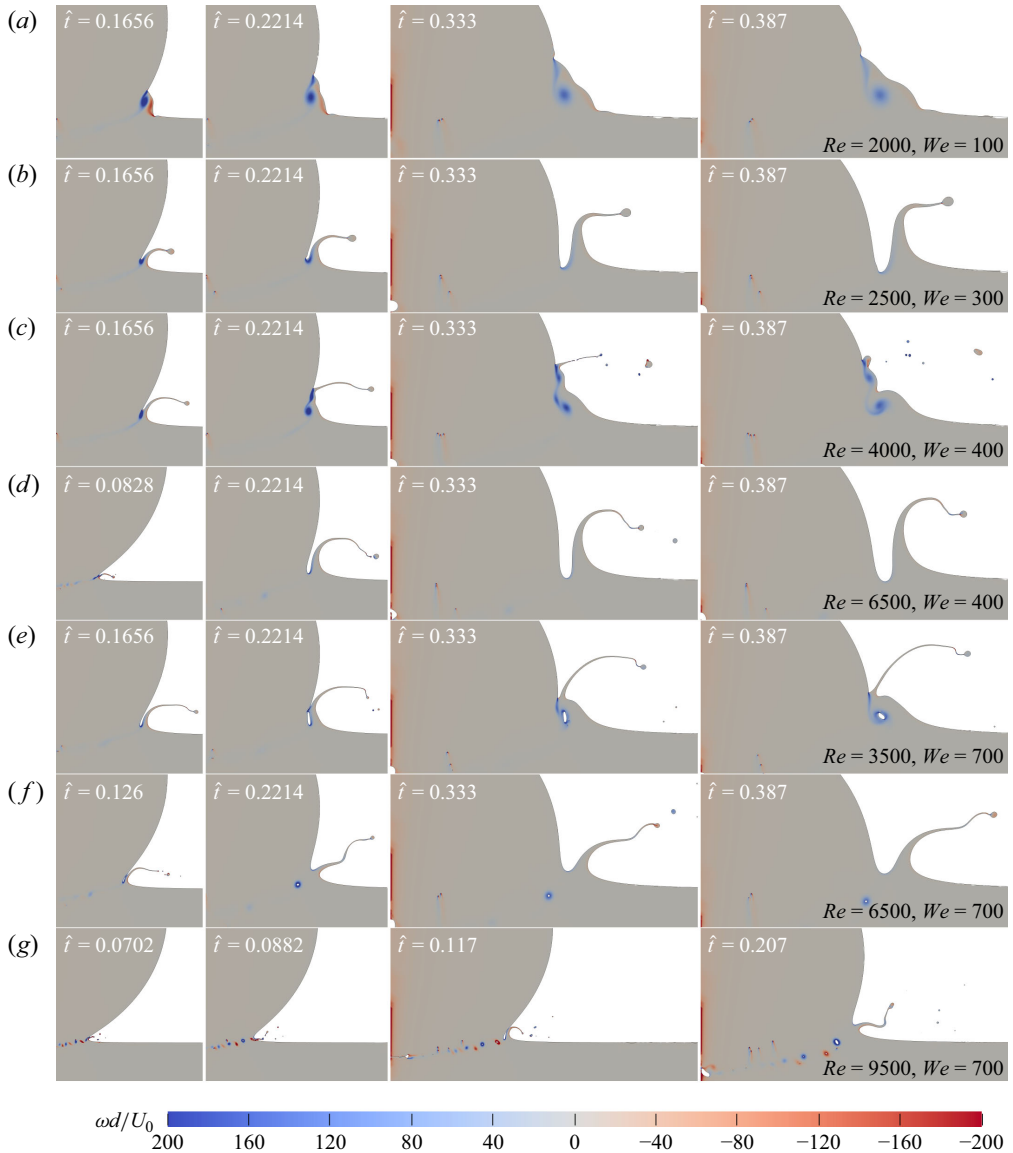


Figure 5. Representative cases calculated under different impact conditions, showing various repeatable jet behaviours and vorticity structures. ω is the vorticity value, where the red and blue colours represent clockwise and counterclockwise rotation, respectively. (a) Coalescence followed by a downward-moving vortex separation ($Re = 2000$, $We = 100$). (b) Combination of ejecta and lamella without vortex separation ($Re = 2500$, $We = 300$). (c) Vortex separation from the upper corner of the ejecta leads to a separated lamella ($Re = 4000$, $We = 400$). (d) Earlier one-sign vortex shedding without separated lamella ($Re = 6500$, $We = 400$). (e) Reconnection between ejecta and drop surface entraps a large toroidal air bubble, leading to a secondary roll jet ($Re = 3500$, $We = 700$). (f) Reconnection between ejecta and drop surface without roll jet, where the entrapped bubble sinks rapidly inside the pool ($Re = 6500$, $We = 700$). (g) Strong interactions between ejecta and free surfaces, resulting in repeated toroidal bubbles and vortex separation ($Re = 9500$, $We = 700$). See supplementary movie 2.

figure 5(b) ($Re = 2500$, $We = 300$) at the same time, the vorticity structure is stronger here and the base of the upper corner is no longer stable, thus transitioning the local dynamics of the ejecta root to a vortex-shedding regime. The detached vortex rings then propagate underneath the free surface in a similar mode to figure 5(a), pushing the ejecta root to climb up along the side of the impact drop. As a consequence, a thicker jet is gradually lifted by the resurfacing vortex due to relatively lower surface tension. The emergence of these two distinct jets has been previously investigated by both experimental (Zhang *et al.* 2012; Agbaglah *et al.* 2015; Sykes *et al.* 2023) and numerical (Agbaglah *et al.* 2015; Sykes *et al.* 2023) works. Following the definition of these authors, the early-emerging jet is hereafter named ‘ejecta’ and the late-emerging jet is named ‘lamella’. In figure 4, this phenomenon is grouped as the \diamond ejecta & lamella regime. As for the lifetime of the initial ejecta, it could be entirely absorbed by the impact drop at relatively low We (Zhang *et al.* 2012) or torn into microdroplets by its outward-stretching leading edge ($\hat{t} = 0.333$ and 0.387 in figure 5c). Figure 5(d) shows the jet dynamics at a slightly higher Re ($Re = 6500$, $We = 400$), where a ‘vortex separation’ event occurs earlier than its counterpart in figure 5(c) ($Re = 4000$, $We = 400$) and the formation of the lamella cannot be clearly observed. Instead, the neck could move rapidly along the radial direction in its early evolution, leaving the vortex ring behind the base of the ejecta.

For relatively higher Weber numbers ($We > 700$) at $Re \approx 3000 \sim 9000$, reconnection between the radial-stretching ejecta and the downward-impinging drop occurs as shown in figures 5(e) and 5(f). The uprising ejecta bends and reconnects with the drop surface at early times before vortex shedding, entrapping and shedding a toroidal bubble at its upper corner. Comparing these two cases, it can be found that the reconnection between ejecta and drop at higher Re (figure 5f) occurs earlier than the case at lower Re (figure 5e). As the angle between the impinging drop and the initial quiescent pool increases with time, the entrapped bubble should become smaller with increasing Re . Indeed, at higher Re (figure 5f), a new neck is established immediately upon the detachment of the toroidal bubble and expands outwards rapidly because of the sharper surface geometry at a small angle between drop and pool, leaving the vortex structure rotating and sinking along the drop–pool interface. In contrast, the bubble is detached at a larger angle at lower Re (figure 5e), where the new point of connection propagates primarily in the vertical direction along the drop surface, and the bubble travels quickly to the outer side of the ejecta base ($\hat{t} = 0.333$) due to pronounced pressure gradient across its curved surface. Accordingly, the motion of the entrapped toroidal bubble leads to different eventual jet dynamics regimes in figure 4: (i) \triangle bumping & roll jet: the toroidal bubble travels to the outer side of the ejecta base, the bubble will resurface and interact with the free surface of the pool, generating a secondary roll jet, and the original ejecta will be completely disintegrated; (ii) ∇ bumping: the bubble sinks quickly enough and stays at the inner side of the ejecta base, the remaining part of the ejecta will keep extending and the original ejecta will not be replaced. A rough limit between these two types of phenomenon is given at $Re \approx 4000$ in figure 4.

In the phenomenon mentioned earlier, the distinction from one to two jets in drop impact has brought attention to a previously overlooked aspect of the phenomenon. According to Agbaglah *et al.* (2015), the emergence of a second jet is determined by whether the vortex detaches from the upper corner of the ejecta base in the parameter range $Re \leq 5000$ and $We \leq 900$. These authors have found that the capillary number $Ca = We/Re = \mu_l U_0 / \sigma$ might be the most appropriate parameter to characterise this transition, and a transitional boundary at $Ca = 0.2$ was concluded to represent the approximate limit of the vorticity-shedding regime. In our current study, a more realistic boundary (red line A1 in figure 4) is introduced to differentiate between the one-jet regime (\circ ejecta) and the two-jet regime

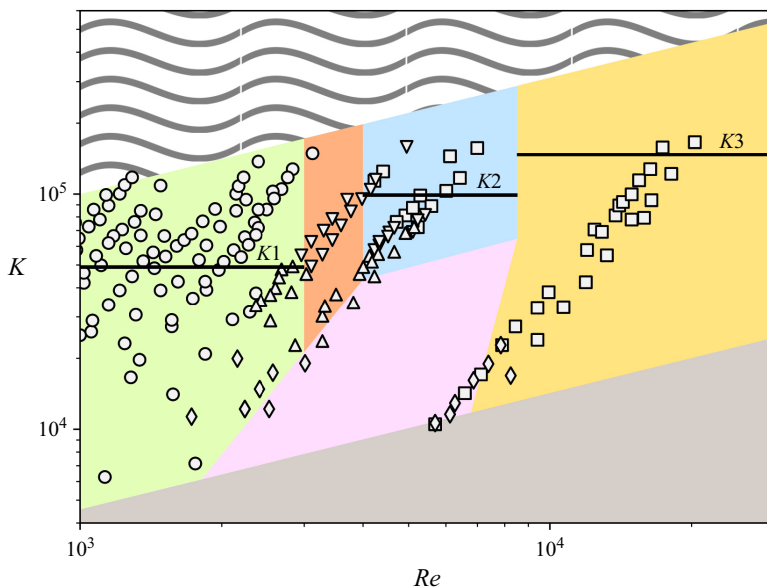


Figure 6. Regime map of drop impact in terms of dimensionless Reynolds (Re) and splashing ($K = We\sqrt{Re}$) numbers. The numerical classifications are shown using the same colour convention as in figure 4. The experimental results reported in Thoraval *et al.* (2012) are plotted with different symbols: ○, smooth ejecta sheet; △, quartering; ▽, bumping; ◇, protrusion; □, irregular splashing. Overlap of distinctive splashing regimes can be found between numerical simulations and laboratory experiments. The wavy region indicates the area not explored in the present numerical simulations.

(◇ ejecta & lamella and △ bumping & roll jet) based on our numerical results, which looks quite close to the $Ca = 0.2$ line, further verifying the validity of the previously established transitional limit.

In the highest range of Reynolds numbers ($Re > 9000$), the phenomenon of continuous vortex shedding becomes prominent (□ irregular splash in figure 4). This behaviour is exemplified in figure 5(g) for a case at $Re = 9500$ and $We = 700$, where the vortex-shedding event occurs much earlier compared with other cases. This early onset of vortex shedding leads to oscillations of the ejecta base immediately after contact. Consequently, the thin ejecta is propelled to bend up and down, resulting in alternating collisions with the surfaces of drop and pool. In this process, toroidal bubbles of alternate signs are entrapped by the newly established neck points and only the leading parts of the ejecta survive and move outwards. As the impact angle increases over time, the bubble entrapment event takes longer to develop, causing the bubble to grow in size until the ejecta is no longer in contact with the interfaces. Eventually, a von-Kármán-type street is formed, characterised by the regular shedding of vortices along the drop-pool interface (Castrejón-Pita *et al.* 2012; Thoraval *et al.* 2012).

In some previous studies, a secondary dimensionless parameter K (splashing number), defined as $K = We\sqrt{Re}$, is also often used to characterise the drop-impact phenomena (Deegan *et al.* 2007; Thoroddsen *et al.* 2011; Thoraval *et al.* 2012). Figure 6 reorganises the current numerical outcomes in terms of the Re and K parameters, and the experimental data from Thoraval *et al.* (2012) are incorporated into the plot using different symbols for reference. Despite some deviations between our numerical set-up and their experiments, superpositions of distinctive splashing behaviours can be clearly observed in these two datasets. Both the ○ ejecta (low Re) and □ irregular splash (high Re) regimes are

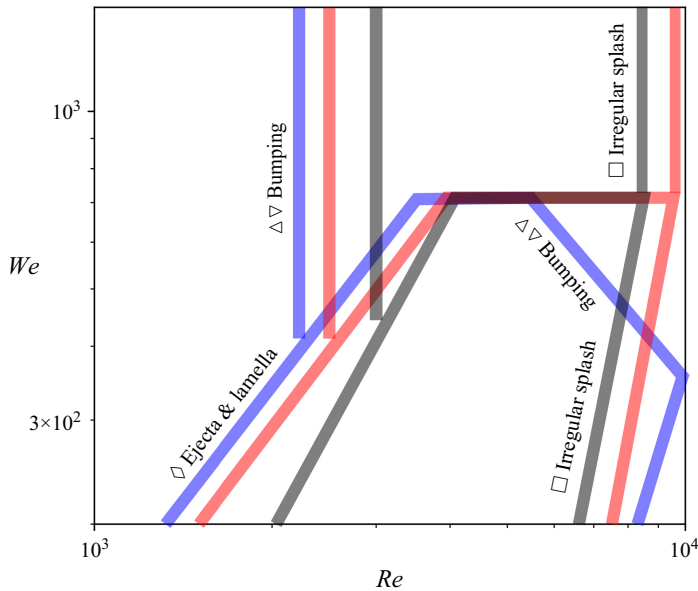


Figure 7. Effect of drop shape variation on the key transition boundaries between different splashing regimes. Three drop shapes are considered: blue, prolate ($\alpha = 1.17$); red, spherical ($\alpha = 1.0$); black, oblate ($\alpha = 0.88$). The numerical classifications follow the same symbol conventions as in figure 4. The combined symbol $\Delta\nabla$ represents a unified ‘bumping’ regime, encompassing both the Δ bumping & roll jet and ∇ bumping regimes, to indicate the reconnection between the ejecta sheet and the drop surface.

found in good alignment between numerical simulations and laboratory experiments. At intermediate Re , the upward protrusion of the ejecta at lower K in the experiment is well captured in the present vortex detaching and resurfacing category (\diamond ejecta & lamella), while the quartering and bumping classes at higher K fall within our toroidal bubble entrapment regimes (Δ bumping & roll jet and ∇ bumping). These results underscore the concordance between our numerical regime map and existing experimental data, further enhancing the reliability of this comprehensive characterisation of drop-impact behaviour.

4.2. Effect of drop shape on transition boundary

As discussed in § 2.3, another key parameter influencing splashing dynamics is the drop shape at the moment of impact. The effect of drop shape on jet formation and bubble entrapment has been highlighted in some previous studies (Thoraval *et al.* 2013, 2016; Li *et al.* 2018), indicating its potential to shift regime boundaries in splashing behaviour. Following the approach of Thoraval *et al.* (2013), the effective drop diameter is defined as $d = (d_v d_h^2)^{1/3}$, and the drop shape is characterised by the aspect ratio $\alpha = d_v/d_h$, where d_v and d_h denote the vertical and horizontal diameters, respectively. Figure 7 presents additional simulations conducted with varying aspect ratios α for $1000 \leq Re \leq 10\,000$ and $200 \leq We \leq 1500$, spanning the key regime boundaries while keeping the effective drop diameter constant. Three drop shapes were examined: prolate ($\alpha = 1.17$), spherical ($\alpha = 1.00$) and oblate ($\alpha = 0.88$). These simulations suggest that drop shape plays a subtle yet non-negligible role in influencing the transition boundaries. At high Reynolds numbers ($Re > 6000$), a systematic rightward shift of the \square irregular splash transition boundary is observed as α increases from 0.88 (black) to 1.00 (red). For the prolate drop ($\alpha = 1.17$, blue), this trend continues, further suppressing the occurrence of \square irregular splash in the lower-right region of the regime map and expanding the $\Delta\nabla$ bumping behaviour toward

lower We . Figure 8(c) presents an example of high-Reynolds-number impact dynamics at $Re = 10000$ and $We = 800$ for drops with varying aspect ratios. As α decreases, the drop becomes flatter, reducing the inclination angle between the drop surface and the quiescent pool. This flattening enhances the neck curvature, increasing the likelihood of rapidly outward-expanding ejecta root instability. As a result, the neck of the connection becomes increasingly destabilised and the ejecta are more prone to swing, leading to intricate neck dynamics (e.g. von-Kármán-type vortex street) and frequent reconnection with surrounding free surfaces (e.g. chains of bubble rings). Similar behaviours were also reported by Thoraval *et al.* (2013) for impacts at $Re = 12\,900$, where numerical simulations, supported by experimental observations, demonstrated that oblate drops, especially those with flatter bases, tend to produce more complex neck dynamics and pronounced bubble-ring entrapment during the early stages of impact.

On the other hand, in the lower-Reynolds-number range, we observe a leftward shift of both the \diamond ejecta & lamella transition and the $\Delta\nabla$ bumping boundary as α increases (see figure 7). This trend indicates that a more prolate drop shape promotes the formation of a stronger vortex at the upper corner of the ejecta base, thereby facilitating both vortex shedding (associated with \diamond ejecta & lamella) and reconnection events (associated with $\Delta\nabla$ bumping). At low Re , the ejecta typically emerges thicker and advances more slowly compared with high- Re cases due to reduced inertial forces and greater viscous damping. Under such conditions, the redistribution of momentum caused by drop shape becomes more subtle, especially near the ejecta root. Prolate drops focus more of their impact momentum along the vertical axis, thus encouraging the base of the ejecta to turn upward more quickly. More critically, the elongated geometry of a prolate drop enhances the local curvature at the upper corner of the ejecta base as it rises. This sharper curvature brings the ejecta sheet into closer proximity with the descending drop surface, creating favourable conditions for the formation of a strong vortex at the ejecta base. Once generated, this vortex can either detach from the upper corner or exert sufficient force to drive the ejecta base into reconnection with the drop surface, especially at higher Weber numbers, resulting in bubble entrapment as illustrated in figure 8(a). In contrast, oblate drops, with their flatter impact bottom, distribute momentum more radially. This lateral momentum spreading accelerates the horizontal expansion of the ejecta base while delaying its vertical deflection. Although the root of the ejecta eventually transitions from horizontal to vertical growth due to the intrinsic dynamics of sheet propagation, this progression leads to distinct behaviours near the regime transition boundaries for oblate drops. As illustrated in figures 8(a) and 8(b), when the drop shape shifts from prolate to spherical at lower Re and higher We , the reconnection point between the ejecta and the drop surface moves outward in the radial direction, resulting in a larger entrapped toroidal bubble. For an oblate drop ($\alpha = 0.88$), the reduced vertical momentum and delayed deflection can even prevent the ejecta sheet from making contact with the descending drop surface altogether, thereby suppressing reconnection and shifting the $\Delta\nabla$ bumping transition boundary further to the right.

These shape-dependent effects, though subtle, meaningfully influence the boundaries between splashing regimes, underscoring the importance of accounting for drop geometry in impact analyses and related applications. Given the difficulty in precisely controlling drop shape in experiments and limited understanding of its role in altering impact phenomenon and transitional dynamics, these numerical insights could provide a valuable foundation for future investigations and furthermore offer guidance for interpreting complex splashing behaviours and for optimising operating conditions in applications such as inkjet printing and additive manufacturing, where drop deformation is often inevitable and impactful.

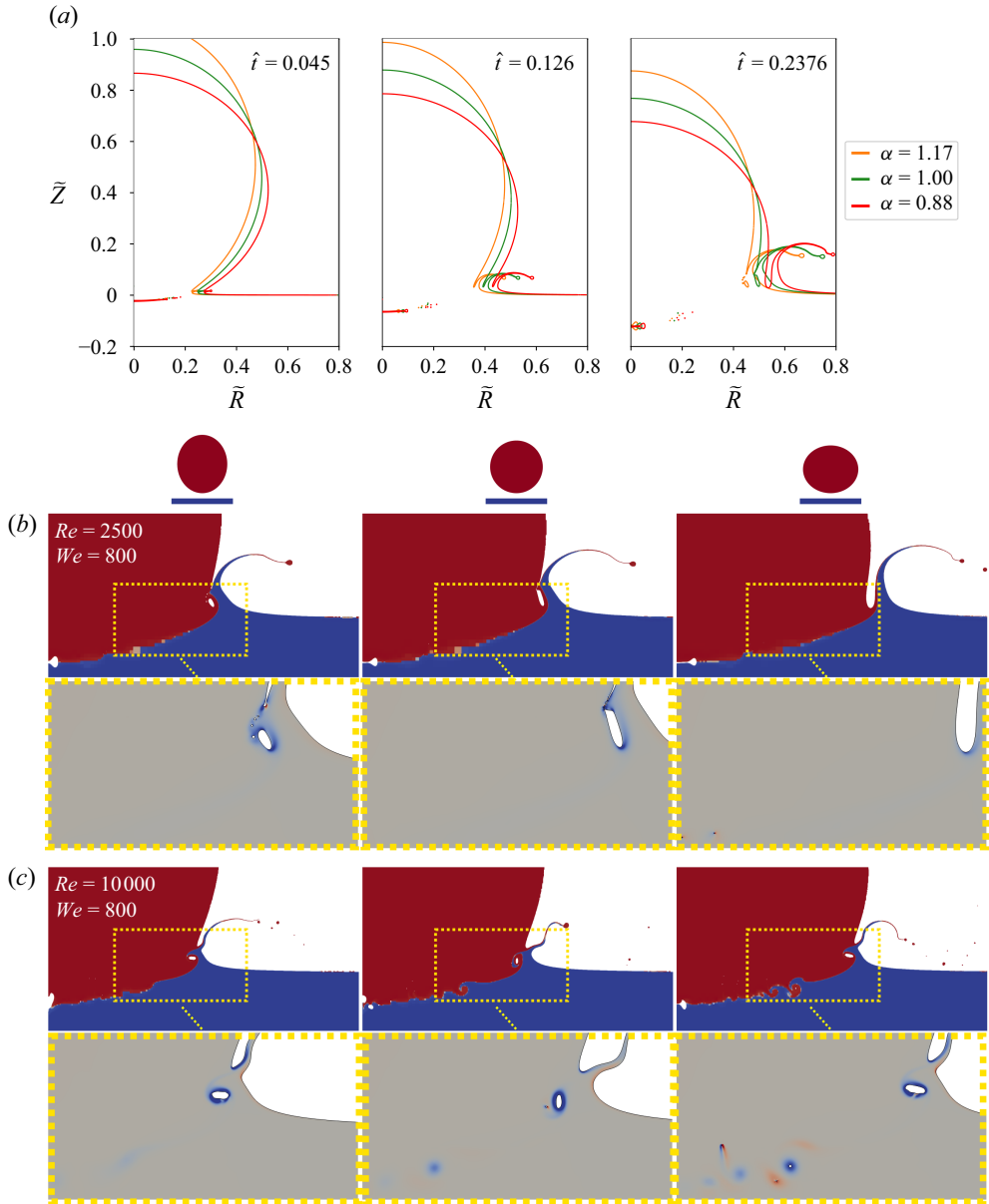


Figure 8. Early-time impact dynamics for drops with varying aspect ratios at $\alpha = 1.17, 1.00, 0.88$, while maintaining a constant effective drop diameter. (a) Gas–liquid interface evolution over time (left to right) at $Re = 2500$, $We = 800$. (b) Neck dynamics at $\hat{t} = 0.2376$ for $Re = 2500$, $We = 800$. (c) Neck dynamics at $\hat{t} = 0.171$ for $Re = 10\,000$, $We = 800$. In the top panels of (b) and (c), red and blue denote liquid originating from the drop and the pool, respectively. In the bottom panels of (b) and (c), red and blue indicate clockwise and counterclockwise vorticity in the zoomed regions. Insets show the initial drop shape (not to scale).

4.3. From corolla to BC

Another interesting aspect of the drop impact process is the overall evolution of the crater-shaped structure. Figure 9 presents typical examples of different modes of crater evolution for a constant Reynolds number ($Re = 18\,000$) observed in our simulations, with variations in the Weber number (see supplementary movies 3–6). The left part of each snapshot

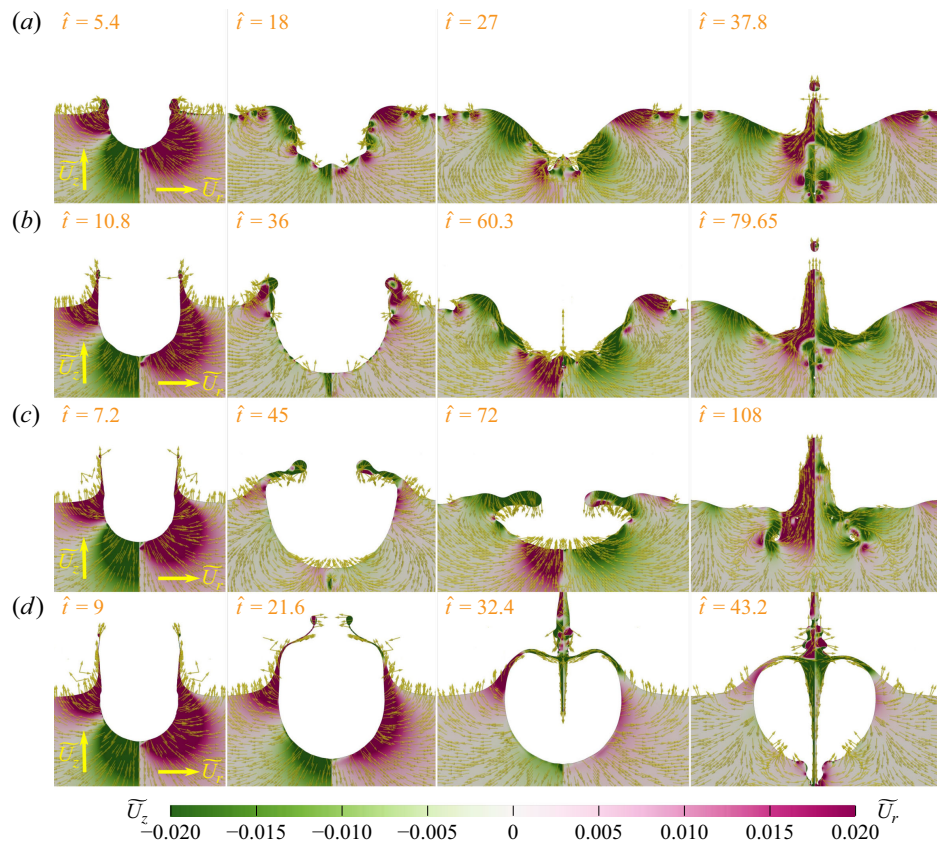


Figure 9. Direct numerical simulation snapshots for $Re = 18\,000$, illustrating different drop-impact dynamics and flow field under varied Weber numbers: (a) $We = 200$, thick tongue with central Worthington jet; (b) $We = 800$, crown with Worthington jet; (c) $We = 1300$, semiclosed dome with Worthington jet; (d) $We = 2000$, BC. For each snapshot, the left part shows the magnitude of axial velocity \tilde{U}_z and the right part shows the magnitude of radial velocity \tilde{U}_r , where the purple colour means positive and the green means negative. See supplementary movies 3–6.

shows the magnitude of axial velocity \tilde{U}_z and the right part shows the magnitude of radial velocity \tilde{U}_r , where the purple colour means positive and the green means negative. In figure 9(a), where the liquid has the highest surface tension, the growth of the crown is greatly suppressed, resulting in the formation of a thick tongue (swell) and a U-shaped cavity ($\hat{t} = 5.4$). Due to the substantially low inertial force to the surface force, the structure reaches its maximum position quickly after impact and undergoes contraction caused by the concentric propagation of capillary waves along the crater wall ($\hat{t} = 18$). At higher We (figure 9b), the crown is more developed and the structure maintains a longer expanding period before collapsing. Further increasing We , as shown in figure 9(c), a thinner liquid crown is captured and its upper parts bend at higher elevations. In the second frame of figure 9(c) ($\hat{t} = 45$), where the cavity just reaches its maximum depth, it can be clearly observed that both \tilde{U}_z and \tilde{U}_r are negative in the upper crown, indicating that the crown is collapsing towards the impact axis. Notably, in this case, cavity contraction initiates from the shallowing of the cavity bottom rather than the propagation of capillary waves coming from the earlier collapsing crown. For the highest range of We , the crown ultimately necks in as illustrated in figure 9(d), encapsulating a large bubble and forming a central ‘bullet jet’, the same as the case experimentally validated in § 3.

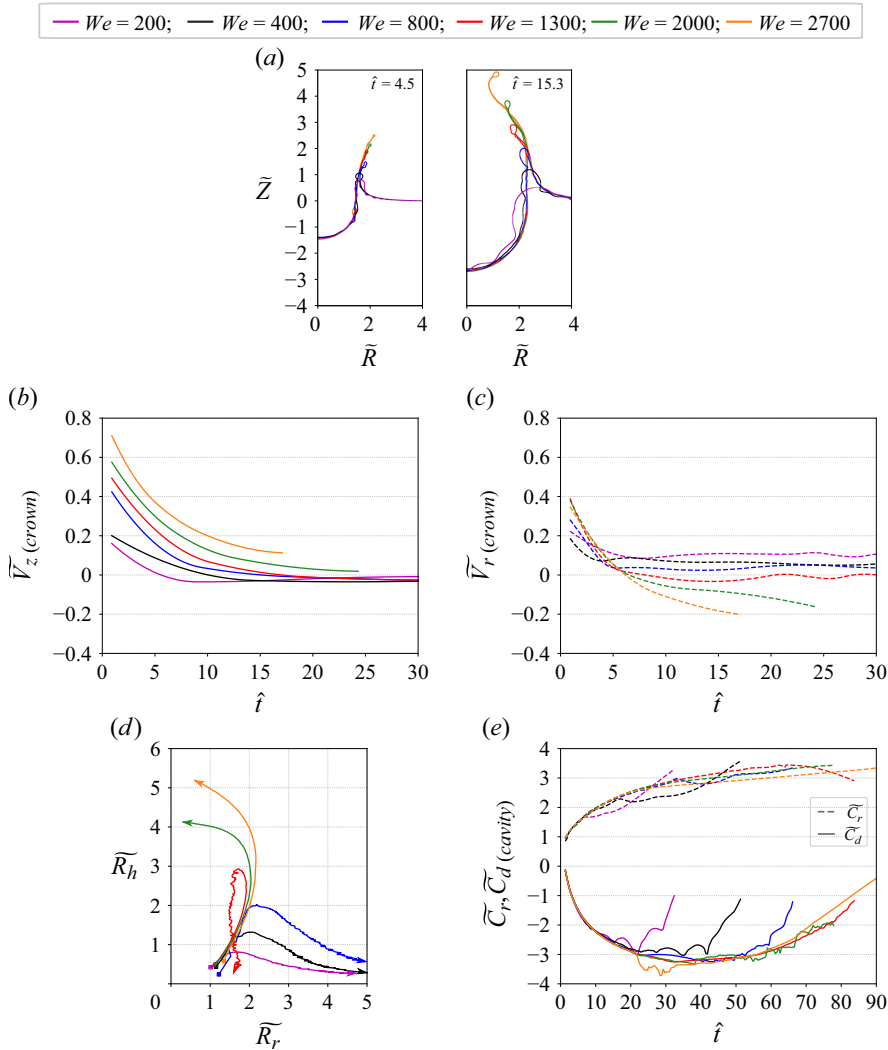


Figure 10. Effect of Weber number on the main crater of drop impact at $Re = 18\,000$. (a) Gas–liquid interface shape at $\hat{t} = 4.5$ and 15.3 . See supplementary movie 7. (b) Time evolution of the axial velocity of the crown tip, obtained by differentiating a smoothed spline fit to its tracked position. (c) Time evolution of the radial velocity of the crown tip, obtained by differentiating a smoothed spline fit to its tracked position. (d) Trajectories of the crown rim. The square marks the start point at $\hat{t} = 0.9$ and the arrow points at the direction of the motion. (e) Time evolution of the cavity width (dashed lines) and depth (solid lines).

Figure 10(a) illustrates the effect of Weber number on the evolution of the main crater. Upon varying the liquid surface tension, a clear pattern emerges: lower surface tension (higher We) leads to a faster, higher and thinner crown (see supplementary movie 7). Under high We , the upper crown surges and expands rapidly, experiencing significant effects from the surrounding airflow (refer to figure 12b and discussion in § 4.4), causing it to bend towards the impact axis. In contrast, surface tension minimally affects the cavity during its initial stage ($\hat{t} = 4.5$), although its impact becomes more pronounced once the crown collapses ($\hat{t} = 15.3$) (see also figure 10e). This phenomenon is particularly evident in cases with smaller Weber numbers ($We = 200$ and 400), where propagation of capillary

waves at later times reduces the dimensions of the cavity, leading to the collapse of the structure.

Figures 10(b) and 10(c) show the time evolution of the axial (\tilde{V}_z) and radial (\tilde{V}_r) velocities of the crown tip, obtained by differentiating a smoothed spline fit to its tracked position. The higher the We , the larger the \tilde{V}_z . At low We , the stronger surface tension significantly hinders the axial rise of the crown. This can be observed by the earlier time point when \tilde{V}_z approaches zero, where the crown reaches its maximum height and retracts shortly after impact. Conversely, the \tilde{V}_r curves corresponding to higher We values ($We = 1300, 2000$ and 2700) decrease more rapidly and subsequently become negative, signifying the inward-bending activities of its thinner upper crown. Figure 10(d) depicts the trajectories of the crown rim for different Weber numbers. For relatively low We , the crown grows similarly, retracting vertically after reaching its maximum height while expanding radially (see figure 9a,b). However, for high We , as showcased in figure 9(d), the crown rises faster and grows thinner, which allows its upper part to warp towards the impact axis before reaching the maximum height, leading to the eventual BC closure. Interestingly, for a case with intermediate Weber number at $We = 1300$ (see figure 9c), the crown, despite its inward-bending tendency, fails to enclose. Instead, it attains a maximum height and subsequently undergoes inward collapse. The negative values for both \tilde{V}_z (red curve in figure 10b) and \tilde{V}_r (red curve in figure 10c) in the later stage signify that the rim continues to slowly approach the z -axis as it descends, where it rejoins the shallowing cavity before complete merger. In figure 10(e), the temporal evolution of the dimensionless cavity width (dashed lines \tilde{C}_r) and depth (solid lines \tilde{C}_d) is presented. For smaller We , the effect of surface tension is more significant, preventing the further expansion of the cavity. Here we see the less smooth curves for lower We cases showing more pronounced effects of surface wave propagation on the cavity evolution.

The progressive effects of We on the crown evolution reveal the presence of a distinct threshold that marks the initiation of BC phenomenon. Pan *et al.* (2008) first reported a non-monotonic transitional boundary in terms of We and dimensionless film thickness $\tilde{h} = H/d$ for the onset of bubble encapsulation during water drop impacting thin water films. They observed a decrease in the transitional We with an increase in \tilde{h} when the film thickness is smaller than the crater size. For impact on deep pools ($\tilde{h} \geq 2$), a constant characteristic boundary $We \approx 2570$ was identified for the BC phenomenon. By compiling previous experimental data in the literature, Murphy *et al.* (2015) concluded the occurrence of BC at $We > 2000$ for low-viscosity liquids. A similar value of $We \approx 2450$ was later obtained by Sochan *et al.* (2018) in their study on splashing shapes in different liquid systems. In addition, these authors observed that the transitional We limit in high-viscosity liquid may become significantly larger than in low-viscosity liquid, highlighting the influential role of liquid viscosity in the closure phenomenon. However, due to the limited range of examined liquids (petrol, water and diesel fuel), detailed effects and dependence of transitional We on Re were not able to be fully elucidated.

In our current numerical investigations, as shown in figure 4, BC formation is observed across all calculated ranges of Re when We surpasses a certain threshold, signifying the dominance of inertial forces over the surface tension forces. The Weber number are explored for $100 \leq We \leq 3000$, corresponding to surface tension values in the range of $\sigma \approx 72.14 \sim 2164.33 \times 10^{-3} \text{ N m}^{-1}$ in realistic experimental conditions. Generally, the BC starts to be found at $We > 900$. However, the onset of the ultimate liquid crown depends primarily on the final status of the leading jet, and the occurrence of BC shows great dependence on the types of early-time jet dynamics due to liquid viscosity variations, so they do not adhere to a single scaling relationship. Therefore, as indicated in figures 4 and 6, by employing the simple relation $K = We\sqrt{Re}$, three transitional boundaries that

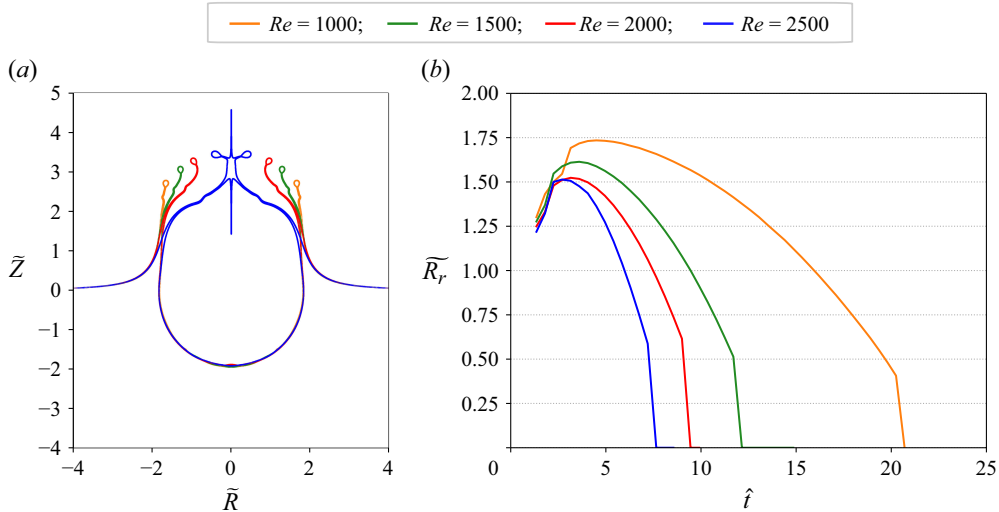


Figure 11. Effect of Reynolds number on the main crater of drop impact at $We = 2000$ within the \bigcirc ejecta early-time splashing regime. (a) Gas-liquid interface shape at $\hat{t} = 7.65$. (b) Time evolution of the radius of the upper crown (\tilde{R}_r).

indicate the onset of BC can be determined by fitting our numerical results. Line $K1 = 4.9 \times 10^4$ separates the BC phenomenon at low Re within the \bigcirc ejecta regime (figure 5b), line $K2 = 9.9 \times 10^4$ indicates the onset of BC during ∇ bumping regime (figure 5f), and finally line $K3 = 14.7 \times 10^4$ signifies the occurrence of canopy for the most energetic \square irregular splash regime (figure 5g).

Figure 11(a) shows the effect of varying Reynolds number Re on the impact phenomenon. Here we specifically focus on the \bigcirc ejecta regime ($Re < 3000$) without involving complex early-time splashing interactions between the ejecta and the free surfaces. At higher Re , the crown rises faster, and its upper part subsequently bends inward toward the impact symmetry, resulting in an earlier surface closure as shown in figure 11(b). In contrast, at lower values of Re , viscous forces increasingly counteract liquid inertia, resulting in reduced jet rising velocities. The enhanced viscous effect also helps the crown resist the suction effect due to gas rushing (see discussion in the following § 4.4), delaying the bending of the upper portion. As a result, at lower Re (with higher viscosity), the crown takes longer to converge toward the symmetry axis, rises higher, and traps a larger gas bubble volume. This behaviour potentially explains the dependence of the bubble closure We threshold on Re (corresponding to line $K1$ in figure 4), corroborating prior experimental findings presented by Murphy *et al.* (2015) and Sochan *et al.* (2018) as referenced earlier.

It is noteworthy that the viscosity ratio between the gas and liquid phases is kept constant at $\rho_l/\rho_g = 56$ in the present simulations, meaning that variations in the Reynolds number Re alter both the liquid and gas viscosities simultaneously. This differs from typical experimental conditions in the air, where the gas viscosity remains fixed while only the liquid viscosity changes. In our study, the Reynolds number range is $1000 \leq Re \leq 30\,000$, corresponding to liquid viscosities in the range of $\mu_l \approx 1.00 \times 10^{-3} \sim 30.1 \times 10^{-3} \text{ N s m}^{-2}$ and gas viscosities of $\mu_g \approx 17.9 \times 10^{-6} \sim 536.8 \times 10^{-6} \text{ N s m}^{-2}$. Under typical impact conditions in the air ($\mu_g = 18.1 \times 10^{-6} \text{ N s m}^{-2}$), the viscosity ratio would be in the range $\rho_l/\rho_g = 55 \sim 1660$, making the ambient gas in our simulations effectively more viscous at lower Re . As a result, the increased gas viscosity introduces additional damping effects that could influence crown expansion, closure dynamics and bubble entrapment.

Specifically, higher gas viscosity may increase the drag resistance from the surrounding gas and suppress the growth of the crown, leading to a more confined structure compared with realistic air-based experiments. In three dimensions, the enhanced gas viscosity may dampen instabilities along the crown rim, leading to a smoother, less fragmented transverse rim structure. Additionally, the increased viscous resistance in the gas phase can potentially delay crown closure, eventually resulting in larger entrapped bubbles than those observed experimentally. While the present approach ensures numerical consistency and stability across different Re cases, it is important to recognise that these effects may introduce discrepancies when directly comparing with experiments conducted in the air. Nevertheless, the overall trends observed in our simulations remain valuable for understanding the fundamental mechanisms governing crown formation and closure under varying viscosity conditions. Future studies could explore cases with a fixed gas viscosity to provide a more direct comparison with experimental results.

4.4. Mechanism of surface closure

Surface-sealing phenomena are commonly observed in processes such as water entry of projectiles (Marston *et al.* 2016*b*; Kroeze, Rivas & Quetzeri-Santiago 2023) and oscillating bubble explosion near an interface (Li *et al.* 2019; Rosselló *et al.* 2022), where a splash curtain is forcefully ejected outwards. While several forces, including inertia, surface tension and ambient pressure, have been proposed as driving factors for surface closure (Clanet 2007; Aristoff & Bush 2009; Marston *et al.* 2016*a,b*; Eshraghi, Jung & Vlachos 2020; Wang *et al.* 2022), the intricate interplay among these forces and the dominant mechanism remain a subject of controversy.

To understand the mechanism of surface closure during drop impact, we also need to turn our attention to the intriguing airflow dynamics around the crown. Figure 12 presents detailed airflow information during drop impact, providing numerical insight into the surface closure mechanism. As the liquid crown rises from the surface, external gas rushes into the expanding cavity, causing a reduction in internal pressure ($\hat{t} = 1.8$). Meanwhile, the crown's outward expansion is met with increasing hydrodynamic resistance from the liquid pool, which restricts further lateral displacement. The resulting force balance redirects the crown rim upward, leading to a transition from horizontal to vertical motion ($\hat{t} = 7.2$). As the liquid film continues to expand under the action of inertia, a large vortex (yellow arrow) is generated due to gas rushing and subsequently detaches from the crown rim. This, in turn, results in a low-pressure region within the gradually growing vortex, as indicated by the green arrow at $\hat{t} = 12.6$. For higher We , as shown in figure 12(*b*), the substantial pressure difference between the interior and exterior sides of the crown further compels its thinner film to bend inwards towards the symmetry plane ($\hat{t} = 18$), leading to the eventual bubble closure event ($\hat{t} = 25.2$). During this process, one could expect that the interplay of inertia, surface tension and aerodynamic pressure would significantly influence the behaviour of the thin-walled crown. For a case with lower We in figure 12(*a*), qualitatively similar airflow profiles emerge during its early stages. However, the relatively higher surface tension mitigates the vertical extension of splashes while encouraging the accumulation of liquid at its upper rim, giving rise to a thicker and shorter crown. In these instances, the pressure difference is less dominant in drawing the crown bending, although a slight tendency can be still observed. Instead of surface closure, this crown reaches its maximum position first and immediately undergoes a contraction phase (see also figure 9*b*), leading to the collapse of the structure.

Figure 13(*a*) shows a representative frame captured during high-speed drop impact, illustrating the inward-bending movement of the free-standing liquid film. As the crown

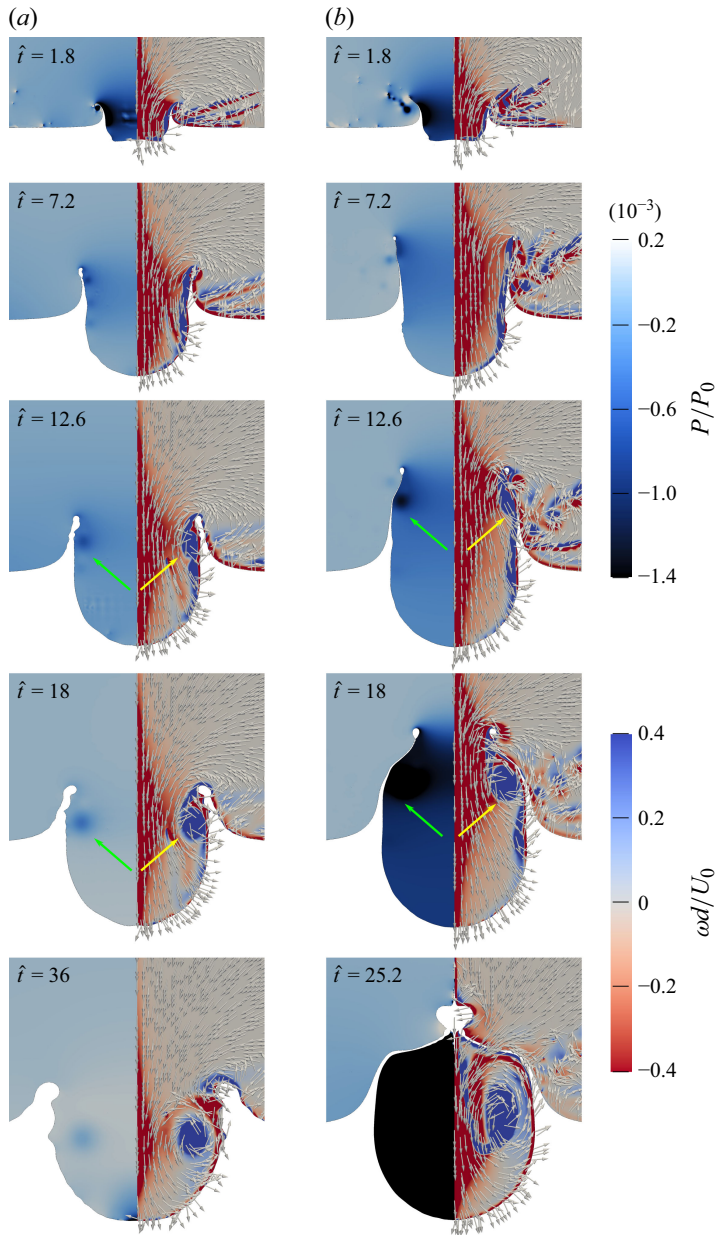


Figure 12. Details of airflow information involved in (a) $Re = 18\,000$ and $We = 800$, open corolla and (b) $Re = 18\,000$ and $We = 2000$, BC formation. The left part shows pressure amplitude and the right part shows vorticity field and flow streamlines. The boundary between coloured and uncoloured regions (white) indicates the gas–liquid interface. The yellow arrow indicates vortex separation due to air rushing, and the green arrow points at the corresponding low-pressure region. The vorticity field is normalised by d/U_0 and the pressure field is scaled by the initial dynamic pressure of the impact drop $P_0 = (\rho_l U_0^2)/2$.

expands, a large vorticity patch is generated around the rim interface due to gas shearing. Figure 13(b) displays the recorded time evolution of the airflow positive vorticity peak (purple arrow in figure 13a) for the two distinct cases presented in figure 12. Initially, the vorticity peak magnitude appears significantly stronger for the case with reduced surface

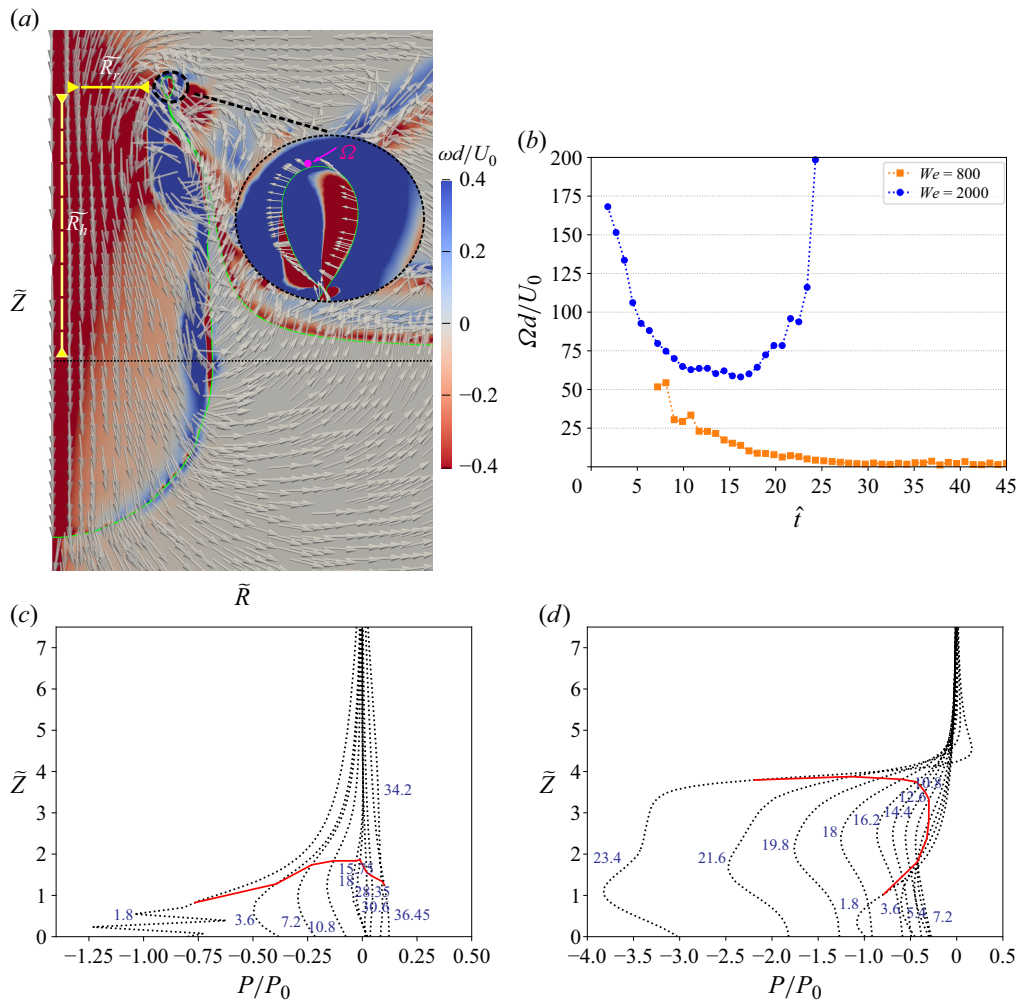


Figure 13. (a) Representative snapshot of velocity field and vorticity structure during high-speed drop impact ($Re = 18\,000$, $We = 2000$). The insert focuses on the flow details near the crown rim. The purple arrow points at the local airflow vorticity peak (Ω). (b) Time evolution of the airflow vorticity peak Ω recorded near the crown rim. The pressure profiles along the axial (symmetry) line at different time instants are plotted for cases (c) $We = 800$ and (d) $We = 2000$. The dimensionless time \hat{t} is marked along each curve. The red curve indicates the locations of rim height \tilde{R}_h .

tension at $We = 2000$. As the structure rises further, its rim decelerates (see figure 10b), and the vorticity is gradually mitigated. Notably, starting from $\hat{t} \approx 10$, the upper crown undergoes rapid inward shrinkage and a high-velocity field is formed near the surrounding gas, resulting in an inflection point for the vorticity peak with a minimum value before surface sealing. In contrast, for the case with higher surface tension at $We = 800$, the rim starts to retract after reaching a maximum position, and the vorticity weakens and vanishes as the structure collapses. In figures 13(c) and 13(d), we plot their pressure profiles along the axial line, with the position of the rim height \tilde{R}_h indicated by red curves. Over time, a rapid drop in aerodynamic pressure can be caused due to surface shrinking before surface closure, while the pressure exhibits a gradual increase in the case with higher surface tension.

These results demonstrate the significant role of aerodynamics in the surface-sealing process during drop impact. Further endeavours should focus on advancing our understanding of this phenomenon under varied liquid properties and ambient environments, unravelling the dominant mechanisms governing the transition from liquid curtain expansion to surface sealing. Particularly, for further delineating the transitional boundary between non-closure and closure, combined parameters that integrate both hydrodynamic and aerodynamic effects will be crucial. This aspect remains to be explored in future work.

5. Conclusion

In this work, we have conducted a thorough exploration of high-speed drop impact dynamics through a series of axisymmetric simulations. Through careful comparisons with existing experimental data, our simulation successfully reproduced most of the phenomena captured by camera, showing its ability and effectiveness to reproduce key splashing features. Our meticulous observations have led to the identification of various repeatable early-time splashing patterns within the jets, vortex and overall crater structures, revealing the intricate nature of high-speed splash. We show that, under increased We , the crown exhibits accelerated growth, reaches greater heights and becomes thinner. This phenomenon facilitates the bending of the crown's upper portion toward the impact axis under further reduced surface tension, leading to the ultimate crown closure event for the highest We range. This observation confirmed the existence of a corolla–canopy transition driven by the combined effects of surface tension and aerodynamic pressure, highlighting the subtle interplay of forces at play. We also demonstrated the crucial role of the delicate balance between inertia, surface tension and aerodynamic forces in governing the surface-sealing process on the thin-walled crown. The comprehensive investigation culminated in the development of a regime map for high-speed drop impact splashes, which encompasses both the early jet dynamics and the overall crater evolution, thereby providing a profound and detailed understanding of this intriguing phenomenon.

Supplementary movies. Supplementary movies are available at <https://doi.org/10.1017/jfm.2025.10543>.

Acknowledgements. We appreciate the beneficial discussions and help from the Basilisk community. Simulations were performed using the computational resources of Advanced Research Computing at Virginia Tech.

Funding. This work is supported by the scholarship from the China Scholarship Council (CSC) under grant CSC no. 201908320462.

Declaration of interests. The authors report no conflict of interest.

Appendix A. Effect of spatial resolution

In this appendix, we examine the effects of grid resolution on the numerical outcomes of drop impact in axisymmetric configurations. The numerical set-ups and impact conditions employed in this analysis are identical to the validated case outlined in § 3 ($Re = 30\,060$, $We = 2964$). Here we vary the maximum mesh refinement level, denoted as L_{max} , from 11 to 17 by utilising the AMR algorithms implemented in the Basilisk code.

A.1. Early-time splashing phenomenon

Figure 14 shows the evolution of the VOF two-phase field with time simulated under different spatial resolutions. Two distinct splashing modes are observed when comparing

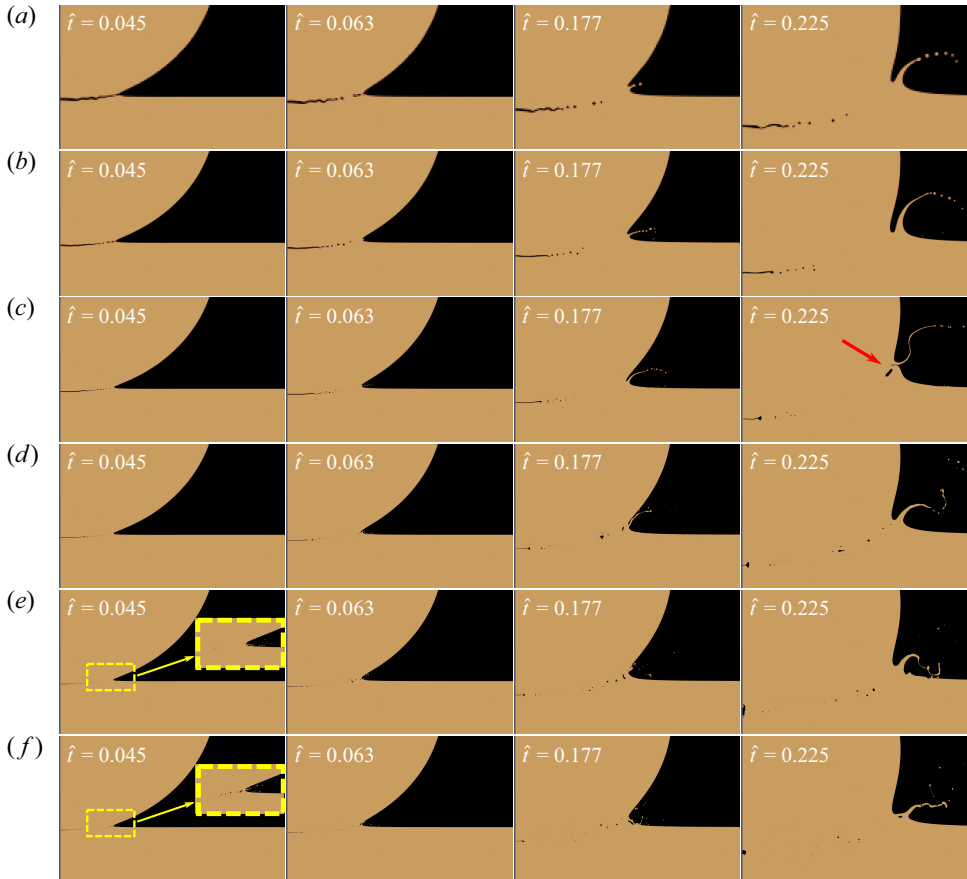


Figure 14. Early-time splashing behaviours captured under different spatial resolutions in axisymmetric configurations ($Re = 30\,060$, $We = 2964$). The snapshots of the VOF two-phase field are demonstrated for (a) $L_{max} = 12$, (b) $L_{max} = 13$, (c) $L_{max} = 14$, (d) $L_{max} = 15$, (e) $L_{max} = 16$ and (f) $L_{max} = 17$. Higher maximum refinement levels (d, e, f) show ‘irregular splash’ and alternate bubble entrapment near the neck region, whereas lower levels (a, b) can only capture the emergence of a smooth ejecta. The results indicate that (c) $L_{max} = 14$ is the resolution limit where the large angle interaction between the uprising ejecta and the downward-moving drop is first captured (red arrow).

the dynamics near the neck region across different resolutions. At finer resolutions ($L_{max} = 15, 16, 17$), strong interactions occur between the radial-stretching jet and the surfaces of the drop and pool. In contrast, coarser resolutions ($L_{max} = 12, 13$) capture only a rising ejecta without secondary jet impingement, due to relatively larger cell size. As for $L_{max} = 14$, the ejecta rises ‘smoothly’ in its early evolution and impinges subsequently to the surface of the downward-moving drop (red arrow at $\hat{t} = 0.225$ in figure 14c), indicating that this is the resolution limit at which the reconnection activities between the ejecta and the drop can be first captured.

The observed approximate convergence of the primary splashing features with increasing resolution suggests that $L_{max} = 15$ (1638 cells per drop diameter) is necessary to capture such high-energy phenomena of ‘irregular splash’ together with toroidal bubble entrapment. As L_{max} increases, the initial ejecta appears earlier and thinner, resulting in even earlier occurrence of alternate bubble entrapment along the drop–pool boundaries, as shown in figure 14(f). Similar patterns of alterations in the splashing morphology

with varying maximum refinement levels have been also observed in our previous three-dimensional simulations in Wang *et al.* (2023).

It is noteworthy that physical processes of irregular splash and bubble entrapment have been also numerically observed by Thoraval *et al.* (2012) and later been confirmed by Castrejón-Pita *et al.* (2012) using advanced experimental techniques. In the numerical study of Thoraval *et al.* (2012, 2013), they found that irregular splash and bubble (ring) entrapment occur at relatively high Reynolds numbers ($Re > 12\,000$). Despite the smaller range of their study in comparison with our present case, their results suggest that more complex jet dynamics and bubble entrapment can be even expected at higher Re . Furthermore, using the Gerris code (ancestor of the current employed Basilisk code), these authors concluded that a minimum cell size of more than 1000 times smaller than the drop diameter is essential to capture the jet impingement activities (bumping), which agrees well with the resolution limit at $L_{max} = 14$ (820 cells per diameter) observed in this investigation (figure 14c). However, for observing the intricate irregular splash and bubble entrapment occurring at the highest range of Re and We numbers, finer spatial resolution is suggested by both our (figure 14d,e,f) and their (their supplemental material) convergence studies.

A.2. Crater shape and closure event

Figures 15(a) and 15(b) compare the shapes of the air–water interface at $\hat{t} = 0.693$ and $\hat{t} = 1.701$ calculated at different maximum refinement levels. At low resolutions ($L_{max} = 12, 13$), the ejecta rises smoothly from the neck, resulting in an upward-expanding crown rim. At $L_{max} = 14$, the evolution of the crown is significantly altered by the entrapped toroidal air bubble (see also figure 14c). However, for higher resolutions ($L_{max} = 15, 16$ and 17), the expansion of the crown rim is upwards and outwards, which is consistent with previous experimental observations in Murphy *et al.* (2015), as discussed in § 3. It should be noted that the thickness of the early jet can be very thin on its tip and the liquid layer might be represented by just several cells, which makes the shape of the liquid layer close to the tip very sensitive to any changes in numerical parameters. This effect can cause small variations at the tip of the crown (black arrow in figure 15a), but the main shape of the crown is well converged at $L_{max} = 15, 16$ and 17.

Figure 15(c) shows the closure time of the upper part of the crown \hat{t}_c and figure 15(d) shows the volume of the entrapped large bubble V_b at the moment of canopy enclosure, calculated under different maximum refinement levels. Large variations of the closure event are observed when spatial resolution is insufficient. For cases at $L_{max} = 15, 16$ and 17, the results are very close to each other.

A.3. Energetics

Now we discuss the numerical convergence with respect to energetics. The kinetic energy E_k and the gravitational potential energy E_g are calculated as follows:

$$E_k = \frac{1}{2} \int_V \rho \|\mathbf{U}\|^2 dV, \quad E_g = \int_V \rho \mathbf{g} z dV - E_{g0}. \quad (\text{A1})$$

where g is the gravitational acceleration and Z is the vertical distance to the bottom of the computational domain. The integrals are evaluated over the entire liquid phase. Here, E_{g0} is the gravitational potential energy of the liquid phase at $\hat{t} = 0$. The total mechanical energy of the liquid phase is therefore calculated as $E_m = E_k + E_g$. Figure 16(a) plots the time evolution of E_k , E_g and E_m calculated under different maximum refinement levels.

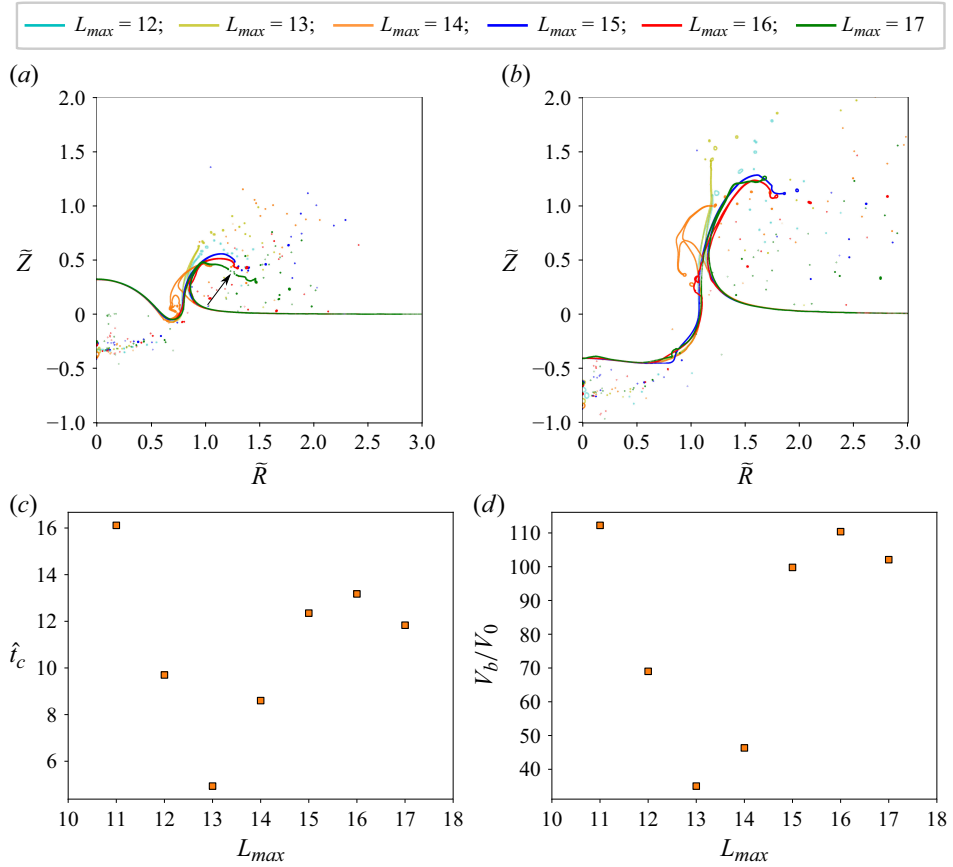


Figure 15. Comparisons of numerical results under different maximum mesh refinement levels in axisymmetric configurations. Panels (a) and (b) compare the shapes of air–water interface at $\hat{t} = 0.693$ and $\hat{t} = 1.701$. The black arrow points at the breakup of the crown tip with the highest resolution. (c) Closure time of the upper part of the crown \hat{t}_c . (d) Volume of the entrapped large bubble V_b at the moment of canopy enclosure, where V_0 is the initial volume of the impact drop.

The results at $L_{max} = 15$, 16 and 17 are well converged, whereas the results at lower levels show large variations.

Figure 16(b) shows the time evolution of the instantaneous dissipation rate calculated directly using the form

$$\epsilon = \int_V \mu \frac{\partial u_i}{\partial x_j} \frac{\partial u_j}{\partial x_i} dV. \quad (\text{A2})$$

where u_i and u_j are the velocity components, x_i and x_j are the 2D spacial components. Comparing all the curves, we see different dissipating patterns between ‘smooth ejecta’ and ‘irregular splash’. For $L_{max} = 15$, 16 and 17 cases, the data exhibit the same qualitative features and magnitudes of early-time dissipation rate, reflecting the rapid transfer of kinetic energy during the chaotic process of the irregular splash. The calculated dissipation rate is generally higher as L_{max} increases, which is reasonable since Basilisk is not energy-conserving by construction and the direct calculation of dissipation rate based on the deformation tensor is greatly dependent on grid resolutions (see also discussion in Mostert & Deike (2020)).

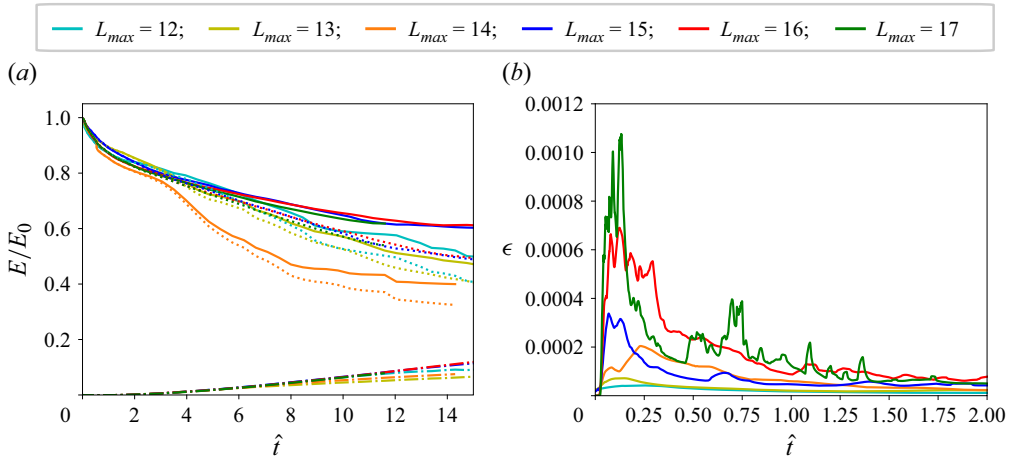


Figure 16. Time evolution of energy aspects calculated under different maximum mesh refinement levels in axisymmetric configurations. (a) Time evolution of kinetic energy E_k (dotted), gravitational potential energy E_g (dashed) and the total mechanical energy $E_m = E_k + E_g$ (solid). In the vertical axis, various energy aspect E is rescaled by the initial kinetic energy E_0 in the domain. (b) Time evolution of instantaneous dissipation rate ϵ collected during simulations.

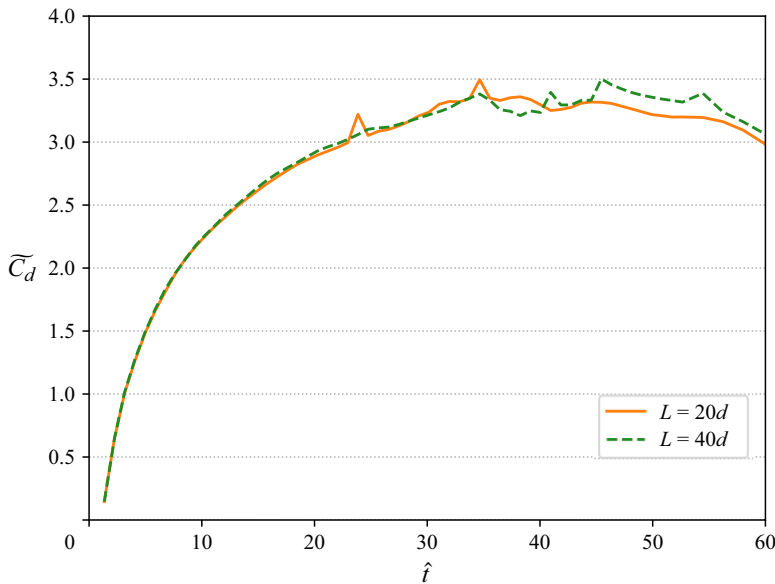


Figure 17. Effect of computational domain size on the cavity depth evolution for drop impact at $Re = 30\,060$ and $We = 2964$.

Appendix B. Effect of computational domain size

Figure 17 shows the effect of computational domain size on the cavity depth evolution for a case at $Re = 30\,060$ and $We = 2964$. In this comparison, the actual domain size $L = 20d$ employed in the main text and a further increased domain $L = 40d$ are examined. While the domain size is doubled, the maximum refinement level is also adjusted from $L_{max} = 15$ for $L = 20d$ to $L_{max} = 16$ for $L = 40d$, in order to maintain the same minimum resolved

scale. The two curves are almost identical, except for minor deviations at later stages after surface closure. These slight discrepancies appear in thin flow structures such as crown tip, central jet and surface capillary waves due to the dynamic mesh refinement using AMR, which does not interfere with the overall cavity expansion. The curves are similar to those in figure 3(f), capturing the same physics and showing no significant difference between the two domain sizes. In both simulations, the maximum cavity depth is reached at $\hat{t} \approx 40$, corresponding to 33 % and 16.5 % of the pool depth for $L = 20d$ and $L = 40d$, respectively. This analysis confirms that the chosen domain size of $L = 20d$ is sufficient for accurately modelling the physical dynamics of the expanding cavity in the present study.

REFERENCES

- AGBAGLAH, G., THORAVAL, M.-J., THORODDSEN, S.T., ZHANG, L.V., FEZZAA, K. & DEEGAN, R.D. 2015 Drop impact into a deep pool: vortex shedding and jet formation. *J. Fluid Mech.* **764**, R1.
- ALJEDAANI, A.B., WANG, C., JETLY, A. & THORODDSEN, S.T. 2018 Experiments on the breakup of drop-impact crowns by Marangoni holes. *J. Fluid Mech.* **844**, 162–186.
- ARISTOFF, J.M. & BUSH, J.W.M. 2009 Water entry of small hydrophobic spheres. *J. Fluid Mech.* **619**, 45–78.
- ASSOULINE, S. 2004 Rainfall-induced soil surface sealing: a critical review of observations, conceptual models, and solutions. *Vadose Zone J.* **3** (2), 570–591.
- BENTHER, J.D., PELAEZ-RESTREPO, J.D., STANLEY, C. & ROSENGARTEN, G. 2021 Heat transfer during multiple droplet impingement and spray cooling: review and prospects for enhanced surfaces. *Intl J. Heat Mass Transfer* **178**, 121587.
- BERBEROVIĆ, E., VAN, H., NILS, P., JAKIRLIĆ, S., ROISMAN, I.V. & TROPEA, C. 2009 Drop impact onto a liquid layer of finite thickness: dynamics of the cavity evolution. *Phys. Rev. E* **79** (3), 036306.
- BISIGHINI, A., COSSALI, G.E., TROPEA, C. & ROISMAN, I.V. 2010 Crater evolution after the impact of a drop onto a semi-infinite liquid target. *Phys. Rev. E* **82** (3), 036319.
- BOUROUBA, L. 2021 The fluid dynamics of disease transmission. *Annu. Rev. Fluid Mech.* **53**, 473–508.
- BREITENBACH, J., ROISMAN, I.V. & TROPEA, C. 2018 From drop impact physics to spray cooling models: a critical review. *Exp. Fluids* **59** (3), 1–21.
- CASTILLO-OROZCO, E., DAVANLOU, A., CHOUDHURY, P.K. & KUMAR, R. 2016 On the impact of liquid drops on immiscible liquids. In International Conference on Nanochannels, Microchannels, and Minichannels, vol. **50343**, pp. V001T08A005. American Society of Mechanical Engineers.
- CASTREJÓN-PITA, A.A., CASTREJÓN-PITA, J.R. & HUTCHINGS, I.M. 2012 Experimental observation of von Kármán vortices during drop impact. *Phys. Rev. E* **86** (4), 045301.
- CHAPMAN, D.S. & CRITCHLOW, P.R. 1967 Formation of vortex rings from falling drops. *J. Fluid Mech.* **29** (1), 177–185.
- CLANET, C. 2007 Waterbells and liquid sheets. *Annu. Rev. Fluid Mech.* **39**, 469–496.
- COPPOLA, G., ROCCO, G. & DE LUCA, L. 2011 Insights on the impact of a plane drop on a thin liquid film. *Phys. Fluids* **23** (2), 022105.
- DASOUI, A.A., YEOM, G.-S. & MURPHY, D.W. 2021 Bursting bubbles and the formation of gas jets and vortex rings. *Exp. Fluids* **62** (1), 1–18.
- DEEGAN, R.D., BRUNET, P. & EGGERS, J. 2007 Complexities of splashing. *Nonlinearity* **21** (1), C1.
- DEKA, H., RAY, B., BISWAS, G., DALAL, A., TSAI, P.-H. & WANG, A.-B. 2017 The regime of large bubble entrapment during a single drop impact on a liquid pool. *Phys. Fluids* **29** (9), 092101.
- ENGEL, O.G. 1966 Crater depth in fluid impacts. *J. Appl. Phys.* **37** (4), 1798–1808.
- ENGEL, O.G. 1967 Initial pressure, initial flow velocity, and the time dependence of crater depth in fluid impacts. *J. Appl. Phys.* **38** (10), 3935–3940.
- ESHRAIGHI, J., JUNG, S. & VLACHOS, P.P. 2020 To seal or not to seal: the closure dynamics of a splash curtain. *Phys. Rev. Fluids* **5** (10), 104001.
- FEDORCHENKO, A.I. & WANG, A.-B. 2004 On some common features of drop impact on liquid surfaces. *Phys. Fluids* **16** (5), 1349–1365.
- FERNÁNDEZ-RAGA, M., PALENCIA, C., KEESSTRA, S., JORDÁN, A., FRAILE, R., ANGULO-MARTÍNEZ, M. & CERDÀ, A. 2017 Splash erosion: a review with unanswered questions. *Earth-Sci. Rev.* **171**, 463–477.
- FRANCOIS, M.M., CUMMINS, S.J., DENDY, E.D., KOTHE, D.B., SICILIAN, J.M. & WILLIAMS, M.W. 2006 A balanced-force algorithm for continuous and sharp interfacial surface tension models within a volume tracking framework. *J. Comput. Phys.* **213** (1), 141–173.

- FUDGE, B.D., CIMPEANU, R., ANTKOWIAK, A., CASTREJÓN-PITA, J.R. & CASTREJÓN-PITA, A.A. 2023 Drop splashing after impact onto immiscible pools of different viscosities. *J. Colloid Interface Sci.* **641**, 585–594.
- FUDGE, B.D., CIMPEANU, R. & CASTREJÓN-PITA, A.A. 2021 Dipping into a new pool: the interface dynamics of drops impacting onto a different liquid. *Phys. Rev. E* **104** (6), 065102.
- FUSTER, D. & POPINET, S. 2018 An all-Mach method for the simulation of bubble dynamics problems in the presence of surface tension. *J. Comput. Phys.* **374**, 752–768.
- GART, S., MATES, J.E., MEGARIDIS, C.M. & JUNG, S. 2015 Droplet impacting a cantilever: a leaf-raindrop system. *Phys. Rev. Appl.* **3** (4), 044019.
- GEPPERT, A., CHATZIANAGNOSTOU, D., MEISTER, C., GOMAA, H., LAMANNA, G. & WEIGAND, B. 2016 Classification of impact morphology and splashing/deposition limit for n-hexadecane. *Atomiz. Sprays* **26** (10).
- GIELEN, M.V., SLEUTEL, P., BENSCHOP, J., RIEPEN, M., VORONINA, V., VISSER, C.W., LOHSE, D., SNOEIJER, J.H., VERSLUIS, M. & GELDERBLUM, H. 2017 Oblique drop impact onto a deep liquid pool. *Phys. Rev. Fluids* **2** (8), 083602.
- GILET, T. & BOUROUBA, L. 2015 Fluid fragmentation shapes rain-induced foliar disease transmission. *J. R. Soc. Interface* **12** (104), 20141092.
- GUILDENBECHER, D.R., ENGVALL, L., GAO, J., GRASSER, T.W., REU, P.L. & CHEN, J. 2014 Digital in-line holography to quantify secondary droplets from the impact of a single drop on a thin film. *Exp. Fluids* **55** (3), 1–9.
- HOWISON, S.D., OCKENDON, J.R., OLIVER, J.M., PURVIS, R. & SMITH, F.T. 2005 Droplet impact on a thin fluid layer. *J. Fluid Mech.* **542**, 1–23.
- JIAN, Z., CHANNA, M.A., KHERBECHÉ, A., CHIZARI, H., THORODDSEN, S.T. & THORAVAL, M.-J. 2020 To split or not to split: dynamics of an air disk formed under a drop impacting on a pool. *Phys. Rev. Lett.* **124** (18), 184501.
- JIAN, Z., JOSSEAND, C., POPINET, S., RAY, P. & ZALESKI, S. 2018 Two mechanisms of droplet splashing on a solid substrate. *J. Fluid Mech.* **835**, 1065–1086.
- JOSSEAND, C., RAY, P. & ZALESKI, S. 2016 Droplet impact on a thin liquid film: anatomy of the splash. *J. Fluid Mech.* **802**, 775–805.
- JOSSEAND, C. & THORODDSEN, S.T. 2016 Drop impact on a solid surface. *Annu. Rev. Fluid Mech.* **48**, 365–391.
- JOSSEAND, C. & ZALESKI, S. 2003 Droplet splashing on a thin liquid film. *Phys. Fluids* **15** (6), 1650–1657.
- KIM, S., PARK, H., GRUSZEWSKI, H.A., SCHMALE, D.G. & JUNG, S. 2019 Vortex-induced dispersal of a plant pathogen by raindrop impact. *Proc. Natl Acad. Sci. USA* **116** (11), 4917–4922.
- KROEZE, T.B., RIVAS, D.F. & QUETZERI-SANTIAGO, M.A. 2023 Gas density influences the transition from capillary collapse to surface seal in microfluidic jet impacts on deep pools. [arXiv:2310.18530](https://arxiv.org/abs/2310.18530).
- LARDIER, N., ROUDIER, P., CLOTHIER, B. & WILLMOTT, G.R. 2019 High-speed photography of water drop impacts on sand and soil. *Eur. J. Soil Sci.* **70** (2), 245–256.
- LENEWEIT, G., KOEHLER, R., ROESNER, K.G. & SCHÄFER, G. 2005 Regimes of drop morphology in oblique impact on deep fluids. *J. Fluid Mech.* **543**, 303–331.
- LHERM, V., DEGUEN, R., ALBOUSSIERE, T. & LANDEAU, M. 2021 Rayleigh–Taylor instability in drop impact experiments. *Phys. Rev. Fluids* **6** (11), 110501.
- LHERM, V., DEGUEN, R., ALBOUSSIERE, T. & LANDEAU, M. 2022 Rayleigh–Taylor instability in impact cratering experiments. *J. Fluid Mech.* **937**, A20.
- LHUISSIER, H., SUN, C., PROSPERETTI, A. & LOHSE, D. 2013 Drop fragmentation at impact onto a bath of an immiscible liquid. *Phys. Rev. Lett.* **110** (26), 264503.
- LI, E.Q., THORAVAL, M.-J., MARSTON, J.O. & THORODDSEN, S.T. 2018 Early azimuthal instability during drop impact. *J. Fluid Mech.* **848**, 821–835.
- LI, T., ZHANG, A., WANG, S.-P., LI, S. & LIU, W.-T. 2019 Bubble interactions and bursting behaviors near a free surface. *Phys. Fluids* **31** (4), 042104.
- LIANG, G. & MUDAWAR, I. 2016 Review of mass and momentum interactions during drop impact on a liquid film. *Intl J. Heat Mass Transfer* **101**, 577–599.
- LIU, X. 2018 Experimental study of drop impact on deep-water surface in the presence of wind. *J. Phys. Oceanogr.* **48** (2), 329–341.
- LOHSE, D. 2022 Fundamental fluid dynamics challenges in inkjet printing. *Annu. Rev. Fluid Mech.* **54**, 349–382.
- MANSOOR, M.M., MARSTON, J.O., VAKARELSKI, I.U. & THORODDSEN, S.T. 2014 Water entry without surface seal: extended cavity formation. *J. Fluid Mech.* **743**, 295–326.

- MARSTON, J.O. & LI, C. 2019 Jet dynamics during vaporization of water drops in hot oil films. *Exp. Therm. Fluid Sci.* **109**, 109873.
- MARSTON, J.O., MANSOOR, M.M., THORODDSEN, S.T. & TRUSCOTT, T.T. 2016a The effect of ambient pressure on ejecta sheets from free-surface ablation. *Exp. Fluids* **57**, 1–10.
- MARSTON, J.O., TRUSCOTT, T.T., SPEIRS, N.B., MANSOOR, M.M. & THORODDSEN, S.T. 2016b Crown sealing and buckling instability during water entry of spheres. *J. Fluid Mech.* **794**, 506–529.
- MEDWIN, H., NYSTUEN, J.A., JACOBUS, P.W., OSTWALD, L.H. & SNYDER, D.E. 1992 The anatomy of underwater rain noise. *J. Acoust. Soc. Am.* **92** (3), 1613–1623.
- MICHON, G.-J., JOSSEAND, C. & SÉON, T. 2017 Jet dynamics post drop impact on a deep pool. *Phys. Rev. Fluids* **2** (2), 023601.
- MOHAMED-KASSIM, Z. & LONGMIRE, E.K. 2004 Drop coalescence through a liquid/liquid interface. *Phys. Fluids* **16** (7), 2170–2181.
- MOREIRA, A.L.N., MOITA, A.S. & PANAÓ, M.R. 2010 Advances and challenges in explaining fuel spray impingement: how much of single droplet impact research is useful? *Prog. Energy Combust. Sci.* **36** (5), 554–580.
- MOSTERT, W. & DEIKE, L. 2020 Inertial energy dissipation in shallow-water breaking waves. *J. Fluid Mech.* **890**, A12.
- MOTZKUS, C., GENSDARMES, F. & GÉHIN, E. 2009 Parameter study of microdroplet formation by impact of millimetre-size droplets onto a liquid film. *J. Aerosol Sci.* **40** (8), 680–692.
- MUKHERJEE, S. & ABRAHAM, J. 2007 Crown behavior in drop impact on wet walls. *Phys. Fluids* **19** (5), 052103.
- MURPHY, D.W., LI, C., D’ALBIGNAC, V., MORRA, D. & KATZ, J. 2015 Splash behaviour and oily marine aerosol production by raindrops impacting oil slicks. *J. Fluid Mech.* **780**, 536–577.
- OKAWA, T., SHIRAIISHI, T. & MORI, T. 2006 Production of secondary drops during the single water drop impact onto a plane water surface. *Exp. Fluids* **41** (6), 965–974.
- OSAMA, M., DEEGAN, R.D. & AGBAGLAH, G.G. 2024 Mass transfer during drop impact on a thin film. *J. Fluid Mech.* **997**, A15.
- PAN, K.-L., CHENG, K.-R., CHOU, P.-C. & WANG, C.-H. 2008 Collision dynamics of high-speed droplets upon layers of variable thickness. *Exp. Fluids* **45** (3), 435–446.
- PAN, K.-L. & HUNG, C.-Y. 2010 Droplet impact upon a wet surface with varied fluid and surface properties. *J. Colloid Interface Sci.* **352** (1), 186–193.
- PANAÓ, M.R.O. & MOREIRA, A.L.N. 2005 Flow characteristics of spray impingement in PFI injection systems. *Exp. Fluids* **39** (2), 364–374.
- Popinet, Stéphane & collaborators 2013–2025 Basilisk. Available at: <https://basilisk.fr>.
- PROSPERETTI, A. & OGUZ, H.N. 1993 The impact of drops on liquid surfaces and the underwater noise of rain. *Annu. Rev. Fluid Mech.* **25** (1), 577–602.
- RAY, B., BISWAS, G. & SHARMA, A. 2015 Regimes during liquid drop impact on a liquid pool. *J. Fluid Mech.* **768**, 492–523.
- REIN, M. 1993 Phenomena of liquid drop impact on solid and liquid surfaces. *Fluid Dyn. Res.* **12** (2), 61–93.
- RIBEIRO, D., SILVA, A.R.R. & PANÃO, M.R.O. 2023a Criterion for bubble encapsulation on drop impact onto a liquid film. *Phys. Fluids* **35**, 3.
- RIBEIRO, D.F.S., PANÃO, M.R.O., BARATA, J.M.M. & SILVA, A.R.R. 2023b Insights on bubble encapsulation after drop impact on thin liquid films. *Intl J. Multiphase Flow* **164**, 104450.
- RODRIGUEZ, F. & MESLER, R. 1985 Some drops don’t splash. *J. Colloid Interface Sci.* **106** (2), 347–352.
- RODRIGUEZ, F. & MESLER, R. 1988 The penetration of drop-formed vortex rings into pools of liquid. *J. Colloid Interface Sci.* **121** (1), 121–129.
- ROISMAN, I.V., HORVAT, K. & TROPEA, C. 2006 Spray impact: rim transverse instability initiating fingering and splash, and description of a secondary spray. *Phys. Fluids* **18** (10), 102104.
- ROSSELLÓ, J.M., REESE, H. & OHL, C.-D. 2022 Dynamics of pulsed laser-induced cavities on a liquid–gas interface: from a conical splash to a ‘bullet’ jet. *J. Fluid Mech.* **939**, A35.
- ROTH-NEBELSICK, A., KONRAD, W., EBNER, M., MIRANDA, T., THIELEN, S. & NEBELSICK, J.H. 2022 When rain collides with plants – patterns and forces of drop impact and how leaves respond to them. *J. Expl Bot.* **73** (4), 1155–1175.
- SAADE, Y., JALAAL, M., PROSPERETTI, A. & LOHSE, D. 2021 Crown formation from a cavitating bubble close to a free surface. *J. Fluid Mech.* **926**, A5.
- SCARDOVELLI, R. & ZALESKI, S. 1999 Direct numerical simulation of free-surface and interfacial flow. *Annu. Rev. Fluid Mech.* **31** (1), 567–603.
- SCOLAN, Y.-M. & KOROBKIN, A.A. 2001 Three-dimensional theory of water impact. Part 1. Inverse Wagner problem. *J. Fluid Mech.* **440**, 293–326.

- SOCHAN, A., BECZEK, M., MAZUR, R., RYŻAK, M. & BIEGANOWSKI, A. 2018 The shape and dynamics of the generation of the splash forms in single-phase systems after drop hitting. *Phys. Fluids* **30** (2), 027103.
- SONI, S.K., KIRAR, P.K., KOLHE, P. & SAHU, K.C. 2020 Deformation and breakup of droplets in an oblique continuous air stream. *Intl J. Multiphase Flow* **122**, 103141.
- SYKES, T.C., CIMPEANU, R., FUDGE, B.D., CASTREJÓN-PITA, J.R. & CASTREJÓN-PITA, A.A. 2023 Droplet impact dynamics on shallow pools. *J. Fluid Mech.* **970**, A34.
- THORAVAL, M.-J., LI, Y. & THORODDSEN, S.T. 2016 Vortex-ring-induced large bubble entrainment during drop impact. *Phys. Rev. E* **93** (3), 033128.
- THORAVAL, M.-J., TAKEHARA, K., ETOH, T.G. & THORODDSEN, S.T. 2013 Drop impact entrapment of bubble rings. *J. Fluid Mech.* **724**, 234–258.
- THORAVAL, M.-J., TAKEHARA, K., ETOH, T.G., POPINET, S., RAY, P., JOSSEERAND, C., ZALESKI, S. & THORODDSEN, S.T. 2012 von Kármán vortex street within an impacting drop. *Phys. Rev. Lett.* **108** (26), 264506.
- THORODDSEN, S.T. 2002 The ejecta sheet generated by the impact of a drop. *J. Fluid Mech.* **451**, 373–381.
- THORODDSEN, S.T., THORAVAL, M.-J., TAKEHARA, K. & ETOH, T.G. 2011 Droplet splashing by a slingshot mechanism. *Phys. Rev. Lett.* **106** (3), 034501.
- TIAN, Y.S., ALJEDAANI, A.B., ALGHAMDI, T. & THORODDSEN, S.T. 2024 Dancing ejecta. *J. Fluid Mech.* **981**, A4.
- VAN HOOFT, J.A., POPINET, S., VAN HEERWAARDEN, C.C., VAN DER LINDEN, S.J.A., DE ROODE, S.R. & VAN DE WIEL, B.J.H. 2018 Towards adaptive grids for atmospheric boundary-layer simulations. *Boundary-Layer Meteorol.* **167** (3), 421–443.
- VOLKOV, R.S., KUZNETSOV, G.V. & STRIZHAK, P.A. 2015 Water droplet deformation in gas stream: impact of temperature difference between liquid and gas. *Intl J. Heat Mass Transfer* **85**, 1–11.
- WANG, H., LIU, S., BAYEUL-LAINÉ, A.-C., MURPHY, D., KATZ, J. & COUTIER-DELGOSHA, O. 2023 Analysis of high-speed drop impact onto deep liquid pool. *J. Fluid Mech.* **972**, A31.
- WANG, J.-X., GUO, W., XIONG, K. & WANG, S.-N. 2020 Review of aerospace-oriented spray cooling technology. *Prog. Aerosp. Sci.* **116**, 100635.
- WANG, Y., WANG, Z., DU, Y., WANG, J., WANG, Y. & CHENGUANG, H. 2022 The mechanism of surface-seal splash during water entry. *Phys. Fluids* **34** (4), 042110.
- WEISS, D.A. & YARIN, A.L. 1999 Single drop impact onto liquid films: neck distortion, jetting, tiny bubble entrainment, and crown formation. *J. Fluid Mech.* **385**, 229–254.
- WORTHINGTON, A.M. 1883 On impact with a liquid surface. *Proc. R. Soc. Lond.* **34** (220–223), 217–230.
- WORTHINGTON, A.M. 1895 *The splash of a drop*. Society for Promoting Christian Knowledge.
- WU, S., ZHANG, J., XIAO, Q. & NI, M.-J. 2021 Comparison of two interfacial flow solvers: specific case of a single droplet impacting onto a deep pool. *Comput. Maths Appl.* **81**, 664–678.
- WU, Y., WANG, Q. & ZHAO, C.Y. 2020 Three-dimensional droplet splashing dynamics measurement with a stereoscopic shadowgraph system. *Intl J. Heat Fluid Flow* **83**, 108576.
- YARIN, A.L. 2006 Drop impact dynamics: splashing, spreading, receding, bouncing. *Annu. Rev. Fluid Mech.* **38** (1), 159–192.
- ZHANG, L.V., TOOLE, J., FEZZAA, K. & DEEGAN, R.D. 2012 Evolution of the ejecta sheet from the impact of a drop with a deep pool. *J. Fluid Mech.* **690**, 5–15.
- ZHOU, Q., LI, N., CHEN, X., XU, T., HUI, S. & ZHANG, D. 2009 Analysis of water drop erosion on turbine blades based on a nonlinear liquid–solid impact model. *Intl J. Impact Engng* **36** (9), 1156–1171.